

Scintillating insights into PSR J0737–3039A and the interstellar plasma of the Gum Nebula from MeerKAT

J. Askew,^{1,2*} D. J. Reardon,^{1,2} R. M. Shannon,^{1,2} M. Bailes,^{1,2} F. Camilo,³ A. Corongiu,⁴ M. Kramer,^{5,6} M. E. Lower,⁷ A. Parthasarathy,^{5,8,9} A. Possenti,⁴ and V. Venkatraman Krishnan,⁵

¹Centre for Astrophysics and Supercomputing, Swinburne University of Technology, P.O. Box 218, Hawthorn, Victoria 3122, Australia

²Australian Research Council Centre of Excellence for Gravitational Wave Discovery (OzGrav)

³South African Radio Astronomy Observatory, 2 Fir Street, Observatory 7925, South Africa

⁴INAF-Osservatorio Astronomico di Cagliari, via della Scienza 5, 09047 Selargius (CA), Italy

⁵Max-Planck-Institut für Radioastronomie, Auf dem Hügel 69, 53121, Bonn, Germany

⁶Jodrell Bank Centre for Astrophysics, University of Manchester, Alan Turing Building, Manchester M13 9PL, UK

⁷Australia Telescope National Facility, CSIRO, Space and Astronomy, PO Box 76, Epping, NSW 1710, Australia

⁸ASTRON, Netherlands Institute for Radio Astronomy, Oude Hoogetveensedijk 4, 7991 PD Dwingeloo, The Netherlands

⁹Anton Pannekoek Institute for Astronomy, University of Amsterdam, Science Park 904, 1098 XH Amsterdam, The Netherlands

Accepted XXX. Received YYY; in original form ZZZ

ABSTRACT

The double pulsar system PSR J0737–3039A/B has enabled some of the most precise tests of strong-field gravity to date. Here, we present a scintillation analysis of the system based on an 18-month observation campaign with the MeerKAT radio telescope. The pulsar radiation shows flux density variations caused multi-path scattering, which results in an interference pattern that varies in frequency and time. We characterise this interference pattern to infer properties of scattering plasma and the orbital geometry of the system. Our preferred model supports a scattering screen located at a distance of $D_s = 360^{+30}_{-40}$ pc. This moderately anisotropic screen of ionized gas (axial ratio $A_R = 2.4 \pm 0.2$) lies near the edge of the Gum Nebula, which is believed to be a supernova remnant (SNR) or an HII region. We estimate the expansion velocity of the nebula to be $V_s = 35 \pm 5$ km s^{−1}, implying a SNR age of $t \approx 1$ Myr. We also constrain the orbital orientation and inclination sense of the double pulsar to be $\Omega = 40^\circ \pm 3^\circ$ and $i > 90^\circ$, respectively. Assuming standard scattering geometry, our model yields a distance estimate consistent with the parallax-derived value of $D = 770 \pm 70$ pc from very long baseline interferometry. We conclude by discussing how future models of pulsar scintillation can enhance our understanding of the IISM and the properties of pulsars embedded within or lying behind such intervening structures.

Key words: (stars:) pulsars: individual: J0737–3039A – methods: data analysis – ISM: individual objects: Gum Nebula – ISM: structure – ISM: supernova remnants – ISM: kinematics and dynamics

1 INTRODUCTION

The pulsar timing technique has led to advancements in fundamental physics, in particular in understanding theories of gravity and general relativity (GR; Kramer et al. 2005, 2006, 2021a; Hu et al. 2022) and equation-of-state physics (EoS; Lattimer & Prakash 2004; Antoniadis et al. 2016; Özel & Freire 2016; Lattimer 2021; Hu & Freire 2024). Breakthroughs have been made especially through the discovery of extreme relativistic binary systems and then studying their orbital orientations and component masses (Hulse & Taylor 1975; Antoniadis et al. 2013; Cromartie et al. 2020; Kramer et al. 2021b). The best tests are made by studying extremely compact orbits with more massive companions (Özel & Freire 2016; Kramer et al. 2021b). The sensitivity and precision of these tests also improve as the number of observations and timing baselines increase. An excellent example of this is the only known double pulsar system,

PSR J0737–3039A/B. The two pulsars (A and B) have rotational periods of 23 ms and 2.8 s, respectively (Lyne et al. 2004). Not only have both neutron stars been detectable, they are in a compact 2.45 hr orbit. This allows for tests of GR with exquisite precision (Kramer et al. 2006).

The mass of components of a binary system can be measured using two post-Keplerian (PK) parameters: the range and shape of the Shapiro delay (Shapiro 1964). This measurement is sensitive to the orbital inclination of the system i , with more ‘edge-on’ systems having stronger constraints on companion mass (Camilo et al. 1994; Shamohammadi et al. 2023). For the double pulsar, the sense of this orientation has not been resolved, with early studies finding $i = 88.1^\circ \pm 0.5^\circ$ (Rickett et al. 2014) but more recent work measuring $i = 90.65^\circ \pm 0.05^\circ$ (Kramer et al. 2021a; Hu et al. 2022; Lower et al. 2024). Determining the geometry and orientation of the double pulsar orbit is important for understanding stellar binary population synthesis models (Stairs et al. 2006; Tauris et al. 2017; Riley et al. 2022), establishing astrophysically motivated priors for kilonova (Zhu &

* E-mail: jaskew@swin.edu.au

Ashton 2020), and calculating when the radio beam of pulsar B will be detectable again (Lyutikov & Thompson 2005; Breton 2009; Perera et al. 2012; Noutsos et al. 2020).

The double pulsar system is also important because it is possible to measure seven PK parameters in the system.¹ The most precise test of gravity comes from the emission of gravitational waves due to orbital period decay (Hulse & Taylor 1975) and is consistent with GR at the 1.3×10^{-4} (95% confidence) level (Kramer et al. 2021a). A systematic error in the orbital period decay is introduced due to the correction for the Shklovskii effect (Shklovskii 1970). The error is caused by the uncertainty in the distance to the double pulsar. Although this error is negligible in current tests of gravity (Kramer et al. 2021a), it will become more significant as timing precision improves (Hu et al. 2020). Currently, measurements in the distance to the system from pulsar timing ($D = 465^{+134}_{-85}$ pc) and very long baseline interferometry (VLBI, $D = 770 \pm 70$ pc) are in slight tension with each other (Kramer et al. 2021a). Both of these methods are purely geometric. The VLBI distance is determined from the semi-annual variations in the apparent position of the image of the pulsar (Gwinn et al. 1986; Ding et al. 2023). The timing distance is inferred from semi-annual variations in pulse arrival times caused by the curvature of the radio wavefront as it passes the orbit of the Earth (Kaspi et al. 1994). It is not uncommon to find differences between the distances determined by pulsar timing and VLBI, potentially caused by several systematic biases (Lutz & Kelker 1973; Verbiest et al. 2012; Ding et al. 2023).

This tension could be resolved by introducing a third independent distance measurement by studying the intensity variations of the scintillation pattern. These variations are caused by scattering from the ionized interstellar medium (IISM) (Rickett & Lyne 1968).

The scattering along the line of sight is often dominated by a particular region of ionized plasma, which can then be approximated as a single dominant screen (Sutton 1971). The propagation of radio waves travelling along different paths results in constructive and destructive interference and variations in intensity in time and frequency. Bright patches in the pattern are known as ‘scintles’. The properties of the scintillation pattern depend on the velocity, structure, and relative distance to this scattering screen (Rickett 1990; Cordes & Rickett 1998). When modelled and accounted for, these properties can be used to infer the distance to a pulsar (Cordes & Rickett 1998; Mall et al. 2022; Reardon et al. 2024a). This model is dependent on the effective velocity along the line of sight, which is a weighted sum of the Earth, scattering screen, and pulsar velocities. The transverse pulsar velocity component is sensitive to the orientation of the orbit and therefore resolves the degeneracy in the sense of the inclination angle from pulsar timing (Ord et al. 2002; Rickett et al. 2014).

We can use also use models of scattering screens to study the velocity, structure, density, and other properties of ionized gas along the line of sight (Mall et al. 2022; Askew et al. 2023; Ocker et al. 2024). These techniques have been applied recently for several structures including those in our local IISM (e.g., within 1 kpc, Mall et al. 2022; Ocker et al. 2024), with a focus on the Local Bubble (an under-dense region in which the Solar system resides, Stinebring et al. 2022; Liu et al. 2023; O’Neill et al. 2024; Stock & van Kerkwijk 2024), the Loop I bubble (Bhat et al. 1998), star-forming nebulae (Gupta et al. 1994; Mall et al. 2022), hot (type O-A) stars (Walker et al. 2017), pul-

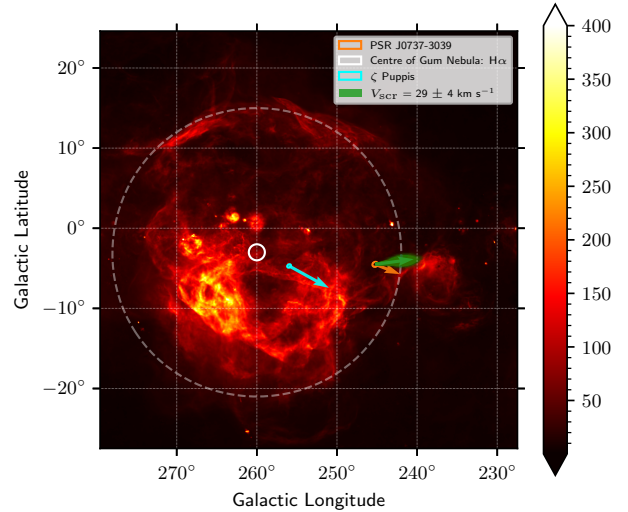


Figure 1. H α emission towards the Gum Nebula and PSR J0737–3039. The colour bar shows the intensity for a given Galactic latitude (y-axis) and longitude (x-axis) in units of $\text{ergs cm}^{-2} \text{sec}^{-1}$. The white 36°-wide dashed circle is centred on the putative centre of the nebula. The cyan ellipse and arrow highlight the star ζ Puppis and its proper motion. The orange ellipse and vector show the location and proper motion of the double pulsar. The green vectors show the screen velocity from our model. The semi-transparent vectors are drawn from the posterior probability distribution to show the uncertainty in the velocity. The emission-line map was produced from the Southern H α Sky Survey Atlas (Gaustad et al. 2001).

sar wind nebulae (Main et al. 2021), and ionized supernova remnant (SNR) shells (Yao et al. 2021).

The Gum Nebula is a noteworthy structure in the Milky Way that has been studied across the electromagnetic spectrum (Gum 1952; Reynolds 1976a; Woermann et al. 2001; Sushch et al. 2011; O’Neill et al. 2024; Wang et al. 2025). It is a complex mixture of overlapping regions of ionized and neutral material that appears close on the sky to the double pulsar (see Figure 1). The Gum Nebula has a large radius of 18°, centred at approximately RA 08:22:53.6 and DEC –42:25:20 (J2000). The distance to the Gum Nebula is still debated, with a range of estimates from 300 to 500 pc (Woermann et al. 2000, 2001; Sushch et al. 2011; Pagani et al. 2012; Purcell et al. 2015; O’Neill et al. 2024). The nebula is thought to have originated as a SNR or HII region (Gum 1952; Reynolds 1976a; Woermann et al. 2000; Sushch et al. 2011; Purcell et al. 2015; O’Neill et al. 2024). If a scattering screen is situated at the edge of the Gum Nebula we could use it to measure the expansion and infer its age, density, and metallicity (Cioffi et al. 1988; Sushch et al. 2011).

This work is the result of an 18-month observing campaign of the double pulsar using the Meer Karoo Array Telescope (MeerKAT). This campaign allowed us to study the properties of the intervening IISM, determine the inclination angle of the binary orbit, and investigate the distance to the system. We describe the data collected with the MeerKAT radio telescope in Section 2. We discuss how we modelled the scintillation, and some of the challenges in modelling in Section 3. The results of this modelling is presented in Section 4. We discuss the implications of our measurements of the orientation of and distance to the system in Section 5. In this section, we also present what we can understand about the ionized gas and physics of the Gum Nebula from our observations. Finally, in Section 6 we

¹ This has enabled incredibly precise mass measurements of the system ($\approx 0.5 M_{\oplus}$; Hu et al. 2022).

Table 1. Properties of the observing bands. Our analysis used 12 observations with the UHF receiver and two observations each using the L-band and S-band receivers.

Observing Band	UHF	L-band	S-band
Central Frequency (MHz)	815.73	1283.58	2187.07
Bandwidth (MHz)	544	856	875
Spectral Resolution (kHz)	33	52	853
No. of Channels	16384	16384	1024

present our main conclusions and discusses ongoing observations of the double pulsar.

2 DATA

2.1 MeerKAT Observations

This work uses data from MeerKAT, a radio interferometer comprising 64, 13.9-m antennas located in the Northern Cape province of South Africa (Jonas & MeerKAT Team 2016). While observations of the double pulsar system have been ongoing since April 2019, the observations used in this analysis extend from June 2022 to November 2023. The observations were taken under the Relativistic Binary programme (RelBin, Kramer et al. 2021b), part of the MeerTime Large Survey Project (Bailes et al. 2020). MeerTime has many aims. These aims include testing theories of gravity, probing neutron star masses in compact binary systems, and using pulsar timing observations to detect nanohertz frequency gravitational waves (Spiewak et al. 2022; Gitika et al. 2023; Miles et al. 2023, 2025).

MeerTime data are recorded using four independent Pulsar Timing User Supplied Equipment (PTUSE) signal processors, which ingest tied-array (voltage) beams produced by the MeerKAT correlator/beamformer (CBF) (Bailes et al. 2020). The CBF produces voltage streams with configurable channelisation. For most pulsar timing projects, a 1024-channel mode is used as it provides lower data rates than other modes, and is designed with a polyphase filter that reduces aliasing artefacts between channels. The PTUSE machines are used in pulsar timing projects to record filterbank (search mode) and fold mode data for searching and timing, respectively (see Bailes et al. 2020, for further details). Our observations were recorded in three observing bands: the UHF-band, L-band, and S-band, which are described in Table 1. To resolve the scintillation in the UHF and L-band observations it is necessary to produce spectra with more than 1024 channels. To accomplish this, in addition to recording data suitable for precision timing, we recorded data simultaneously using a second PTUSE machine. The second PTUSE machine was configured to subdivide each of the 1024 coarse channels by a factor of 16, resulting in 16384 channels. We refer to this data product as the 16 k mode.

For the double pulsar system, the A pulsar (PSR J0737–3039A) is observed by the RelBin theme every month for ~3 hr, which is modestly longer than an entire orbit. This was chosen to deliver two eclipses during the observing campaign, in which the magnetosphere of pulsar B interferes with the radio emission from pulsar A (Lower et al. 2024). The observations were divided into three consecutive scans of duration ~30 min, ~2 hr, and ~30 min respectively.

Table 2. The minimum, mean, and maximum scintillation bandwidths and timescales for each observing band.

Observing Band	UHF	L-band	S-band
Minimum $\Delta\nu_d$ (MHz)	0.036	0.143	0.970
Mean $\Delta\nu_d$ (MHz)	0.070	0.496	3.139
Maximum $\Delta\nu_d$ (MHz)	0.261	1.073	7.876
Minimum $\Delta\tau_d$ (s)	36	46	51
Mean $\Delta\tau_d$ (s)	63	80	130
Maximum $\Delta\tau_d$ (s)	408	410	582

2.2 Dynamic Spectra

The fundamental data products used in this study are dynamic spectra. We first produced these dynamic spectra from MeerPIPE, the pulsar timing data reduction pipeline, which utilises PSRCHIVE pulsar-data processing utility (Hotan et al. 2004). Polarization and flux calibration are also performed on the data during this stage. This calibration is further described in (Serylak et al. 2021). To determine the flux density for each channel and each subintegration, we used the `psrflux` tool, which uses a standard pulse profile derived from pulsar timing as a match filter to measure the flux density with near optimal signal to noise ratio.

The main features of the scintillation pattern in the dynamic spectra are ‘scintles’, which are islands of increased flux density that vary with frequency and time. The decorrelation bandwidth of the scintles rapidly increases with frequency, as seen in Figure 2. The duration of the scintles changes with time as the transverse velocity of the pulsar changes across the orbit (Rickett et al. 2014; Reardon et al. 2019).

3 METHODS

Our analysis uses dynamic spectra taken across 16 epochs spanning 18 months in all three frequency bands. In earlier observations (exclusively obtained at UHF and L band), the 16 k mode was unavailable and therefore the scintillation bandwidth was not resolved in the observations. The dynamic spectra were first divided into sub-dynamic spectra (which we term ‘slices’) of smaller bandwidth and observing time to capture the rapidly changing scintillation bandwidth, $\Delta\nu_d$, (with frequency) and timescale, $\Delta\tau_d$, (with orbital phase).

Rapidly varying scintillation timescale is visually apparent in the dynamic spectra (Figure 2). This motivates the division of the dynamic spectra into windows of time. We chose to divide the windows into 10 min durations as this is longer than the largest measured timescales, as listed in Table 2, while providing uniform sampling across the orbital phase. Windows of different lengths were tested, but provided over-estimation or under-estimation of the scintillation timescale.

In addition, the division of the dynamic spectrum in frequency was necessary due to the large available fractional bandwidth. The difference between the scintillation bandwidth at the top of each band compared to the bottom is ~an order of magnitude (see Figure 2). At each observing band there is also a large amount of scatter in the measurements of $\Delta\nu_d$ used in the analysis (see Table 2 and Figure 4). To account for the evolution of the frequency bandwidth at different bands, the UHF, L-band, and S-band observations were divided into 30 MHz, 50 MHz, and 100 MHz sub-bands, respectively. Some sub-bands were not included in the analysis due to corruption from radio frequency interference (RFI). Notably, the UHF band is nearly devoid of RFI at MeerKAT (Bailes et al. 2020). We only

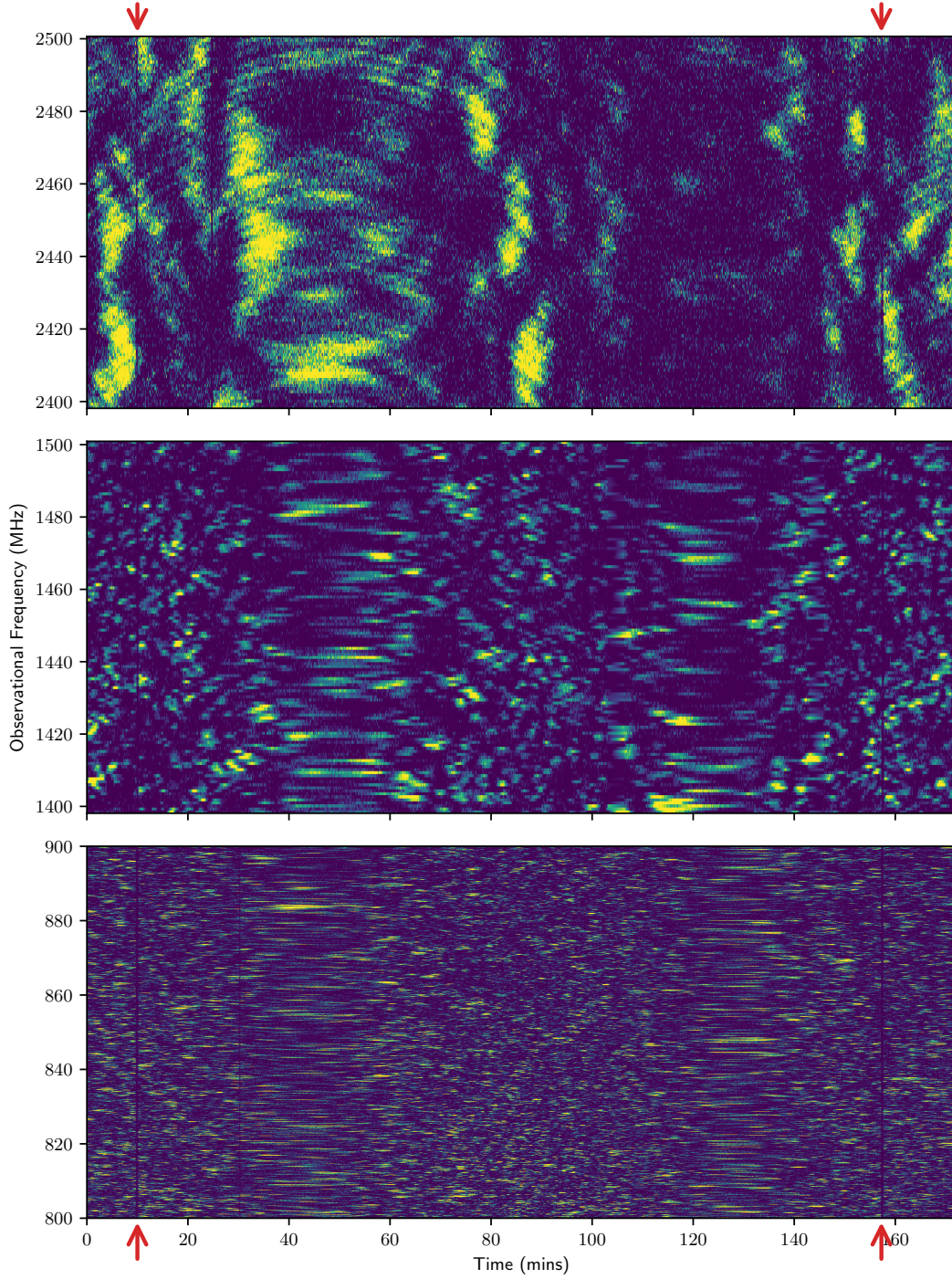


Figure 2. Dynamic spectra of PSR J0737–3039A in S-band (top), L-band (middle), and UHF-band (bottom). Two eclipses, where the beam of pulsar A passes through the magnetosphere of pulsar B, can be seen, marked by the red arrows. The colour scales are all independent across each panel and use linear scaling. The data presented in each panel show a 100 MHz subband. Throughout the work we used the full bandwidth of each observation.

needed to consider removing one sub-band from the data analysis; and even in one case that sub-band was sufficiently clean that it could be used. Measurements of the scintillation properties were thus made in slices comprising sub-bands and windows. The scintillation bandwidth measurements are shown in Figure 4.

At the lowest frequencies observed in UHF (typically below 800 MHz), the scintillation bandwidth is smaller than our 0.033 MHz

spectral resolution. These frequencies were not used in the analysis. In the S-band observations, the scintillation bandwidth was larger than the channel bandwidth in the standard 1024-channel mode, so we did not need to use the 16k-mode dynamic spectra.

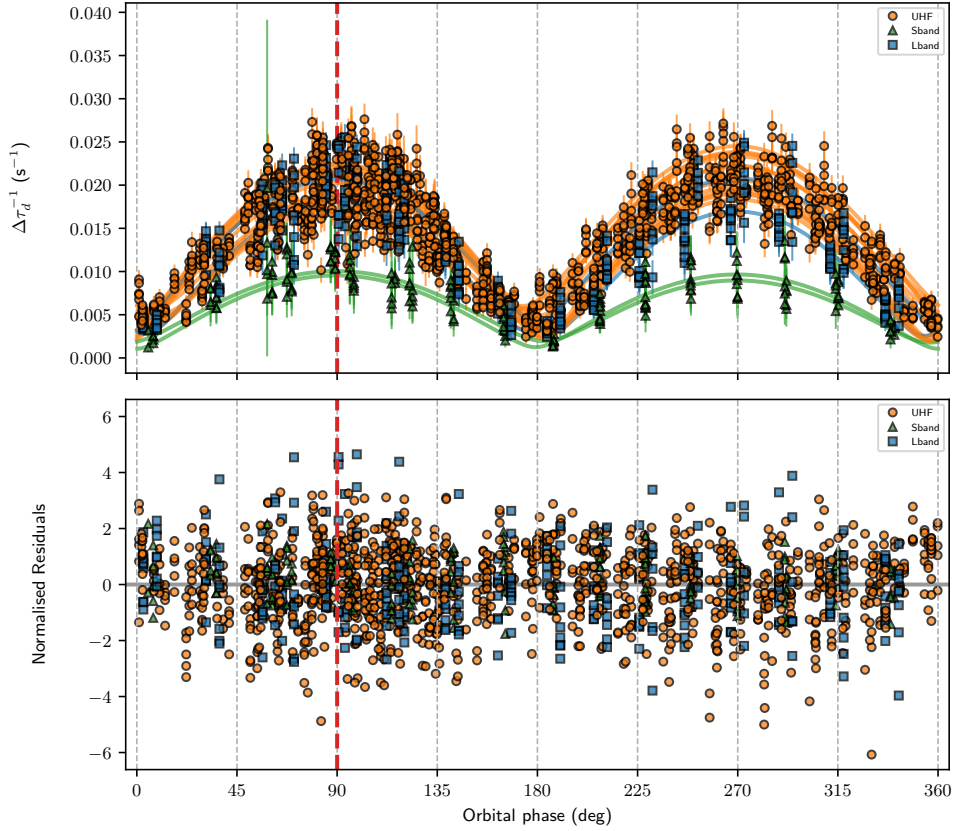


Figure 3. Measurements of, and model for, $\Delta\tau_d^{-1}$. Top panel: Reciprocal of scintillation timescales for UHF (circles), L-band (squares), and S-band (triangles). The solid lines indicate the best-fitting model for \mathbf{V}_{eff} each epoch (16 in total). The maximum a-posteriori parameters for this model are presented in Table 3. Lower panel: Normalised residuals for the best-fitting model. These are the differences between the observations and the model, divided by measured uncertainties. We discuss the whiteness of the residuals in Appendix B. The dashed vertical line indicates the epoch of superior conjunction. Both panels are plotted against the orbital phase of the double pulsar, determined from the true anomaly expressed in degrees (Reardon et al. 2019, Equation A4).

3.1 Scintillation Bandwidths and Timescales

For each slice, we use a two-dimensional (2D) auto-correlation function (ACF) to characterise the scintillation properties. In addition to measuring the scintillation time scale and bandwidth, which measure the bandwidth of the autocorrelation function in time and frequency, we also measure the tilt of the ACF. This is the rotation of the major axis of the ACF ellipse from the time or frequency axes, which can be caused by a large refractive phase gradient in the ISM (Rickett et al. 2014). The rotation is quantified by a gradient ϕ . The 2D ACF is modelled using an analytical function parameterized by $\Delta\nu_d$, $\Delta\tau_d$, and ϕ (Reardon & Coles 2023). Following convention, $\Delta\nu_d$ is defined as the frequency lag at which the correlation falls to one-half its value and $\Delta\tau_d$ is the time lag at which the correlation falls to $1/e$ of the peak value. We measure these properties using the SCINTOOLS² (Reardon 2020) software package. A more detailed description of this fitting method can be found in Rickett et al. (2014) and Reardon & Coles (2023).

During the analysis of the auto-correlation functions, we identified structures that needed to be accounted for prior to making robust estimation of scintillation timescales and bandwidths. Firstly, we identified that the overestimation was caused by an artefact related to the polyphase filters only apparent in the 16-k data. The artefact is an

increase in covariance in the 2D-ACFs at frequency lags 0.520 MHz and 0.832 MHz for UHF and L-band (in the 16 k mode) respectively. This is caused by the polyphase filters in the CBF used to divide the data in 1024 channels. The filters have significant roll-off in sensitivity and signal close to channel edges, introduced to reduce spectral leakage between channels (Bailes et al. 2020). This artefact can cause an overestimation of $\Delta\nu_d$ by $\geq 16\%$ (at UHF).

We also noticed diffuse structures in the ACF: excess signal at high frequency and time lags. We attribute this to a second distinct scintillation pattern. This diffuse structure could be caused by a second scattering screen. In many cases, the phase gradient measured for the second component of the ACF is different (and occasionally orthogonal to) the primary component, which suggests the power is caused by a second screen. Unfortunately, the excess power is too faint to robustly measure scintillation bandwidths and timescales.

To avoid incorrectly biasing our measurements to the presence of the filter artefact or a second scattering screen, we restrict the size of the ACF when performing a fit. In the UHF band, the scintillation bandwidth $\Delta\nu_d$ is smaller (< 0.2 MHz) than the artefact (0.52 MHz). In L-band we use the 1024 channel data to measure $\Delta\nu_d$ where $\Delta\nu_d > 0.832$ MHz and the 16-k data when the scintillation bandwidth is smaller. This results in robust measurements of $\Delta\nu_d$ and $\Delta\tau_d$.

There is also a trade-off between the duration of the window of the dynamic spectra in time and frequency as larger bins lead to more scintles and therefore precise measurement. This trade-off is caused

² <https://github.com/danielreardon/scintools>

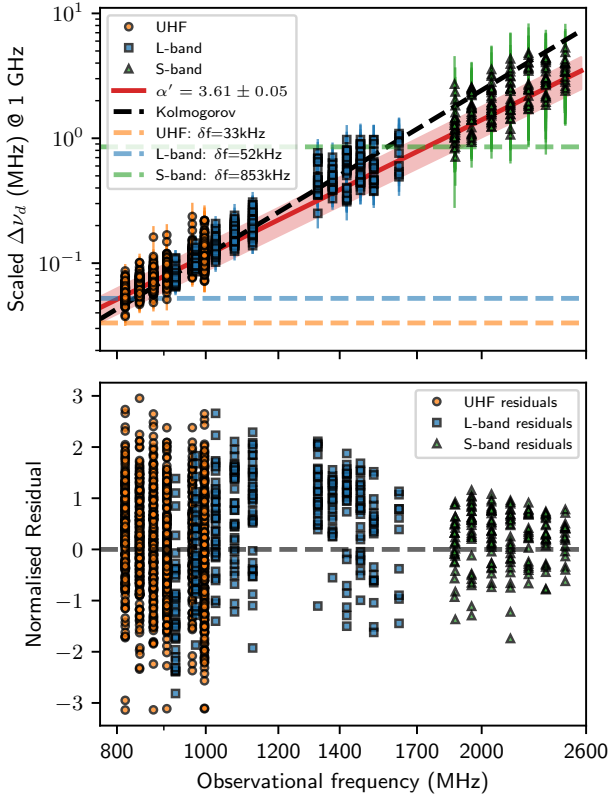


Figure 4. Frequency dependence of scintillation for the double pulsar. The scintillation bandwidth measurements are shown at each epoch in the UHF (circles), L-band (squares), and S-band (triangles) observations. At each epoch, we infer a value for $\Delta\nu_d$. We rescale each epoch with the same median value to account for epoch-to-epoch variations in the scintillation bandwidth. The solid (red) line indicates the globally inferred value for α' and its uncertainty accounting for the variation of $\Delta\nu_d$ between epochs. We also show a global model assuming Kolmogorov turbulence in black. The dashed lines show the channel bandwidth in each observing band. The second panel shows the normalised residuals of this scaled bandwidth (data - model / uncertainty).

by the ‘finite scintle effect’: the ability to precisely measure scintillation bandwidths and timescales depends on the number of scintles in a dynamic spectrum (Cordes 1986). In addition to including standard measurement error, the uncertainties in the scintillation bandwidth and time scale both includes terms that are inversely proportional to the square root of the number of scintles in the dynamic spectrum. For this dataset, however, there is a compromise that needs to be made as larger windows result in biases in our scintillation timescale measurements, as $\Delta\tau_d$ changes rapidly across the orbital phase (as seen in 2). We found that 10 min windows provided a sufficiently large number of scintles and a sufficiently small fraction of the orbit to allow us to both reliably measure scintillation properties, but not be affected by intra-slice orbital variations.

To improve the reliability of error estimation for $\Delta\nu_d$ and $\Delta\tau_d$, we introduce white noise parameters, F and Q , which account for epoch-to-epoch excess noise that could be systematic or astrophysical in origin (Askew et al. 2023). The uncertainty on the measurements

is modified to be

$$\sigma_P = \sqrt{(\sigma_s F)^2 + \left(Q \left(\frac{\nu}{\nu_n}\right)^\xi\right)^2}, \quad (1)$$

where σ_P is the total uncertainty in the measurement, σ_s is the measured uncertainty, F is a scaling factor, and Q is a frequency-dependent quadrature error, measured relative to a reference frequency ν_n (we used 1 GHz) with a spectral exponent ξ . These were modified from Askew et al. (2023) to account for the wider bandwidths of our observations (~ 2 GHz, compared to 300 MHz in Askew et al. (2023)).

While trying to improve ACF fitting, we also explored other methodologies, which were not found to significantly affect the measurements or uncertainties. We considered an alternate method of weighting when fitting a model to the ACF, scaling the uncertainties on the ACF measurements to be proportional to the lag from the centre of the ACF. This was chosen to account for fewer measurements of the ACF at greater lags. However, this only improved the precision of our measurements of the scintillation bandwidth by $\approx 2\%$ (for UHF observations) and did not improve the systematic uncertainties described above. To estimate the uncertainty of $\Delta\nu_d$ and $\Delta\tau_d$, we assume that the 2D-ACF samples are independent, which is a standard practice in scintillation analysis. While the finite scintle effect accounts for correlations between lags from scintillation, other correlated noise sources could introduce correlations in the ACF. We have not considered the impact of this assumption.

3.2 Spectral dependence of scintillation bandwidth

Scintillation is a strongly chromatic process. The degree of chromaticity depends on the structure of the inhomogeneous density fluctuations in the IISM (Lambert & Rickett 1999). These inhomogeneities also impact other properties of the scintillation pattern, including the relationship between scintillation velocity and scintillation bandwidths and timescales (Cordes & Rickett 1998; Lambert & Rickett 1999). Determining how scintillation bandwidth scales with frequency is crucial in establishing a scintillation-based orbital model that can be used to infer the distance to a pulsar.

We model the frequency dependence of the scintillation as a power law with exponent α' , such that

$$\Delta\nu_d \propto \nu^{\alpha'}. \quad (2)$$

The value of the exponent depends on the underlying density fluctuations in the IISM. The electron density power spectrum, $P_{ne}(q; z) \propto q^\beta$, is defined with a power law relationship with the exponent β (Cordes et al. 1986; Rickett 1990; Lambert & Rickett 1999). This exponent can be related to the spectral dependence of the scintillation as

$$\alpha' = \begin{cases} \frac{2\beta}{\beta-2} & \beta < 4, \\ \frac{8}{6-\beta} & \beta > 4, \end{cases} \quad (3)$$

(Bhat et al. 2004). There is no known theoretical relationship between α' and β when $\alpha' < 4$ (e.g., see Figure 16 in Cordes et al. 1986).

We measure the change in $\Delta\nu_d$ as a function of frequency with a global fit to α' across all three observing bands. To determine the scintillation bandwidth at each epoch, we fitted α' using the relationship,

$$\Delta\nu_d = \Delta\nu_{d, 1\text{GHz}} \left(\frac{\nu}{\nu_{\text{ref}}}\right)^{\alpha'}, \quad (4)$$

where $\nu_{\text{ref}} = 1$ GHz.

3.3 Scintillation Velocity

We can infer properties of the transverse motion along the LoS using our measurements from the dynamic spectra. Central to this is the calculation of the scintillation velocity,

$$V_{\text{iss}} = \left[\frac{A_{\text{iss}}}{\text{km s}^{-1}} \right] \left[\frac{D}{\text{kpc}} \frac{\Delta\nu_d}{\text{MHz}} \right]^{1/2} \left[\frac{\nu}{\text{GHz}} \frac{\Delta\tau_d}{\text{s}} \right]^{-1}, \quad (5)$$

where A_{iss} is a constant that relates the screen geometry and density variations to the scintillation pattern speed (Cordes & Rickett 1998). This geometric constant is defined to be

$$A_{\text{iss}} = \left(\frac{c}{4\pi C_1} \right)^{1/2} \left(\frac{C_u}{C_l} \right)^{1/2} \left(\frac{2(1-s)}{s} \right)^{1/2} = A_{\text{iss},5/3,\mu} W_C W_{D,\text{ISS}}, \quad (6)$$

where s is the relative distance to a thin screen of plasma (where $s = 1$ is the position of the Earth, and $s = 0$ of the pulsar), W_C and $W_{D,\text{ISS}}$ are variables that depend on the assumed spatial distribution and relative distance of the intervening plasma. For every LoS one must consider what spatial and spectral models to assume to derive a value of A_{iss} . When deriving a value of A_{iss} , implicit unit conversion is applied to have units of km s^{-1} (Cordes & Rickett 1998). The constant C_1 defines the Fourier relationship between the decorrelation bandwidth, $\Delta\nu_d$, and pulse-broadening timescale, τ_s ,

$$C_1 = 2\pi\Delta\nu_d\tau_s \quad (7)$$

For a uniform distribution of electrons in a Kolmogorov turbulent medium, $C_1 = 0.741$ (Cordes & Rickett 1998; Lambert & Rickett 1999). However, the parameter C_1 depends on the geometric and spectral properties along the LoS. These properties are described in greater detail in Section 4.1.

The methods for determining C_1 (and therefore A_{iss}) from scintillation have not been developed since Rickett et al. (2014), which itself relies on the theory presented in Lambert & Rickett (1999) and Cordes & Rickett (1998). It is therefore not currently possible to calculate values C_1 when $\alpha' < 4$ due to an unknown relationship between α' and β . For completeness, we describe the methodology for determining C_1 and D assuming $\alpha' = 4.4$ in Appendix A.

We can infer properties of the IISM and the orbit of the double pulsar by comparing V_{iss} calculated from the scintillation time scale and bandwidth with a model:

$$\begin{aligned} \mathbf{V}_{\text{eff}}(s) &= (1-s)(\mathbf{V}_p + \mathbf{V}_\mu) + s\mathbf{V}_E - \mathbf{V}_{\text{IISM}} \\ &= \mathbf{V}_{\text{kin}} - \mathbf{V}_{\text{IISM}}, \end{aligned} \quad (8)$$

where \mathbf{V}_p is the transverse component of the orbital velocity of the pulsar, \mathbf{V}_μ is the pulsar transverse space velocity, \mathbf{V}_E is the transverse velocity of the Earth, and \mathbf{V}_{IISM} is the IISM velocity (Cordes & Rickett 1998; Askew et al. 2023). \mathbf{V}_{IISM} is parameterised by its relative velocity in right ascension (RA, α) and declination (DEC, δ): $V_{\text{IISM},\alpha,\delta}$. We measure \mathbf{V}_p , which importantly depends on i and Ω , to be between ≈ 25 and $\approx 315 \text{ km s}^{-1}$ using the timing model from Kramer et al. (2021a). \mathbf{V}_μ has been held fixed using accurate measurements of the proper motion from ($V_{p,\alpha} = -2.47(3)$ and $V_{p,\delta} = 2.04(3)$ Kramer et al. 2021a). \mathbf{V}_E and \mathbf{V}_p are calculated at the epoch of each measurement in the data and fixed at that value.

This velocity model assumes that a thin screen of plasma dominates the scattering along the LoS (Sutton 1971). When modelling $\mathbf{V}_{\text{eff}}(s)$, it is possible to infer the fractional distance to the scattering screen, s , to a few per cent (Reardon et al. 2020; Mall et al. 2022; Ocker et al. 2024; Reardon et al. 2024a), which corresponds to a precision in physical precision of tens to hundreds of pc.

We consider two approaches fitting our model of \mathbf{V}_{eff} to the data.

For the first model (which we will refer to as the $\Delta\tau_d^{-1}$ model), we use the measured scintillation timescales and model the spatial scale,

$$\frac{s_d}{\tau_d} = V_{\text{iss}}, \quad (9)$$

where

$$s_d \equiv A_{\text{iss}} \sqrt{D\Delta\nu_d} \nu^{-1} \quad (10)$$

is the spatial scale, which is the distance over which intensity fluctuations caused by interference become uncorrelated (Rickett 1977; Armstrong et al. 1995; Cordes & Rickett 1998; Lambert & Rickett 1999; Rickett et al. 2014; Reardon et al. 2020)³. At each epoch, the spatial scale is measured relative to a reference frequency of $\nu_n = 1 \text{ GHz}$. The spatial scale for different frequencies at the same epoch can be calculated as

$$s_{d,n} = s_d \left(\frac{\nu}{\nu_n} \right)^\gamma. \quad (11)$$

Using the second model (which we refer to as the V_{iss} model), we derive values for V_{iss} from our scintillation observations using Equation 5. For this model, we scale the frequency dependence bandwidths α' to account for the variations from epoch to epoch. This model can be used to infer posterior distributions of A_{iss} and the distance to the double pulsar D , which are discussed in Section 4.3.

We note that both models use the velocity of the LoS at the Solar System barycentre, which we define to be

$$\mathbf{V}_{\text{LoS}}(s) = \frac{\mathbf{V}_{\text{eff}}(s)}{s}, \quad (12)$$

This is important when comparing our results with other works, as we define the effective velocity at the Earth. All of our models account for anisotropic scattering using methods described in Section 3.5.

3.4 Velocity Modelling with Bayesian Inference

We use Bayesian modelling techniques described in Askew et al. (2023) to infer model parameters and their posterior probabilities. We assume a Gaussian (logarithmic) likelihood. In the case of the $\Delta\tau_d^{-1}$ model, the likelihood has the form

$$\log(\mathcal{L}) = -\frac{N}{2} \log(2\pi\sigma_P^2) - \frac{1}{2\sigma_P^2} \sum_{n=1}^N \left[\frac{s_{d,n}}{\Delta\tau_{d,n}} - \mathbf{V}_{\text{eff},n} \right]^2, \quad (13)$$

where $\Delta\tau_{d,n}$ is the n th measurement of the scintillation timescale from N total measurements, and $s_{d,n}$ is the corresponding inferred spatial scale for this n th measurement. The modelled effective velocity for this measurement is $\mathbf{V}_{\text{eff},n}$. The likelihood used for inference using measurement of V_{iss} has a similar form. In this work, unless explicitly stated, we use uniform priors across the entire (or reasonably broad) parameter spaces in our inferences. When comparing models we can use Bayesian Evidence to select preferred models.

3.5 Assessing Anisotropy

Scattering need not be isotropic. Anisotropic scattering manifests as variations of the scatter-broadened image of the pulsar, approximated as an ellipse, rather than being azimuthally symmetric shape (Cordes et al. 1986; Coles et al. 2005; Rickett et al. 2014; Reardon et al. 2019). In the case of ellipsoidal anisotropy, the image of the

³ This parameter is occasionally referred to as l instead of s_d and is not to be confused with the relative distance to the scattering screen s .

pulsar is broadened non-axisymmetrically, and the anisotropy can be parametrized by an axial ratio A_R and position angle ζ measured East of North of the major axis of the ellipse. Other studies, including those outside pulsar astronomy, indicate anisotropic scattering being dominant along many lines of sight (Desai & Fey 2001; Chandran & Backer 2002; Pen & King 2012; Florinski et al. 2024).

We also consider an extension to this simplest model for anisotropy. This is motivated by a previous study of the double pulsar system (Coles et al. 2005), which used an ellipse to model the observed spatial variations in the scattering from pulsars A and B. They found that while the model was a reasonable fit for the data, the ACF showed additional structure (e.g., Figure 3 of Coles et al. 2005).

As an alternative to an ellipse, we model the scatter-broadened image as a sum of circular harmonics. In a circular harmonic basis, the zeroth degree is a circle, the first is an ellipse, and the second (and higher) degrees are perturbations to that ellipse. We consider perturbations up to the third order. We can define harmonics up to this degree using six parameters, ζ and A_R for the ellipse, Δ_2 and ζ_2 for the second-degree parameters, and Δ_3 and ζ_3 for the third degree. In this notation, $\Delta_{2,3}$ defines the amplitude of the harmonic and $\zeta_{2,3}$ the orientation of the perturbations. The higher-order harmonics allow for a diversity of unique shapes that the IISM could produce due to diffractive or refractive effects in turbulent or intermittent plasma. To remove the unlikely realisations of the circular harmonics with shapes that do not represent a physically motivated scattered-broadened image of the pulsar, we restricted the prior distributions for the amplitude perturbations $\Delta_{2,3} \leq 1$.

This methodology fits nicely into the existing $\Delta\tau_d^{-1}$ model. The perturbed ellipse can be used to calculate a modified spatial scale, $s_{\text{ell}} = s_d r_{\text{ell}}$, which depends on the radial position of the perturbed ellipse, r_{ell} .

4 RESULTS

A summary of our results for the range of models considered is presented in Table 3. The data and model using the best-fitting parameters, for the $\Delta\tau_d^{-1}$ model are shown in Figure 3. We find that a single screen at a relative distance of $s = 0.53^{+0.01}_{-0.02}$ dominates the scattering. For this screen, we measure moderate anisotropy with an axial ratio of $A_R = 2.4 \pm 0.2$ and an anisotropy angle $\zeta = 180^\circ \pm 2^\circ$ East of North. This was supported with $\log(\text{BF}) \approx 72$ compared to an isotropic model. All of the figures in this section, unless otherwise stated, show the results inferred from this model. We also find that this model breaks the degeneracy in the sense of the inclination angle, which pulsar timing is not always sensitive to, with our observations supporting an inclination angle $i > 90^\circ$.

4.1 Spectral and Geometric line of sight properties

Understanding the IISM using scintillation observations can help answer two questions: (1) Where are the electrons along the LoS (i.e., where are the scattering regions)? and (2) How do the inhomogeneities in the IISM impact the scattering at different observing frequencies (i.e., what are the structures of the scattering regions)? A common assumption is that the scattering is caused by electrons with density variations following a Kolmogorov power law ($\alpha' = 4.4$, equivalent to $\beta = 11/3$) residing in geometrically thin screens (Sutton 1971; Cordes et al. 1986; Rickett 1990).

A small change in α' can result in a significantly different physical interpretation of a scattering medium. Previous studies of the frequency dependence of diffractive scintillation have shown that

Table 3. V_{eff} inference. The results presented in this figure use the methods discussed in 3.4 for the $(\Delta\tau_d^{-1})$ and (V_{ISS}) models. Both models support an inclination angle sense of $i > 90^\circ$, assuming the fixed magnitude of inclination angle of $i = 89.65^\circ$ from Kramer et al. (2021a). The differences in ξ , F , and Q are expected due to the different measurements for each model. γ was not inferred within the V_{ISS} model.

Parameter	$\Delta\tau_d^{-1}$	V_{ISS}
i ($^\circ$)	> 90	> 90
Ω ($^\circ$)	40^{+3}_{-3}	52^{+3}_{-3}
s	$0.53^{+0.01}_{-0.02}$	$0.60^{+0.01}_{-0.01}$
$V_{\text{IISM},\alpha}$ (km s^{-1})	-22^{+1}_{-1}	-26^{+3}_{-3}
$V_{\text{IISM},\delta}$ (km s^{-1})	36^{+3}_{-3}	35^{+3}_{-3}
A_R	$2.4^{+0.2}_{-0.2}$	$2.0^{+0.2}_{-0.2}$
ζ ($^\circ$)	180^{+2}_{-2}	169^{+3}_{-3}
γ	$0.69^{+0.03}_{-0.03}$	—
ξ	$-1.7^{+0.5}_{-0.6}$	-6^{+2}_{-2}
F	$2.30^{+0.08}_{-0.08}$	$4.0^{+0.1}_{-0.1}$
Q ($\text{s}^{-1} / \text{km s}^{-1}$)	$6.0^{+0.6}_{-0.7} \times 10^{-4}$	$2.4^{+0.7}_{-0.5}$

spectral indices deviate significantly from those expected from Kolmogorov turbulence. The majority of pulsars show power-law exponents (α') that are shallower than what is expected from Kolmogorov, with the mean estimated to be $\alpha' = 3.9 \pm 0.2$ in Bhat et al. (2004) and median to be $\alpha' = 3.7^{+0.6}_{-0.7}$ in Krishnakumar et al. (2019). We have measured a shallow spectral index for the double pulsar where the scintillation decorrelation bandwidth scales with exponent $\alpha' = 3.61 \pm 0.05$. The data strongly favour $\log(\text{BF}) = 119$ a shallower α' than the value expected of Kolmogorov turbulence because of the large number of measurements involved in the inference (see Figure 4). We note that this is the first measurement of the frequency dependence of scintillation of the double pulsar.

Several potential scattering geometries allow for spectral deviations from that expected from Kolmogorov turbulence. For example, the electron density distribution may follow a power law spectrum with an ‘inner’ or ‘outer’ scale (Lambert & Rickett 1999; Bhat et al. 2004), or there may be a transverse truncation of the scattering screen (i.e., scattering caused by thin sheets folding onto one another, Pen & King 2012; Jow et al. 2024).

We also note that the measurements of $\Delta\nu_{\text{d}, 1\text{GHz}}$ are correlated with flux density (see Figure 5) with the correlation coefficient measured to be ≈ 0.65 . This suggests refractive variations are impacting the diffractive scintillation measurements at each epoch (Shannon & Cordes 2017).

Both Kolmogorov and ‘square-law’ ($\beta = \alpha' = 4$) analytical models have been extensively examined in the literature (Rickett 1990; Lambert & Rickett 1999). We consider modifications to these models that include inner and outer scales defined to be $L_i = \kappa_i^{-1} \text{ m}$, and $L_o = \kappa_o^{-1} \text{ m}$, respectively (Coles et al. 1987; Lambert & Rickett 1999). The inner scale model assumes a Kolmogorov medium that dissipates at a length scale L_i at which kinetic energy begins heating the plasma (Lambert & Rickett 1999) and suppressing the turbulent

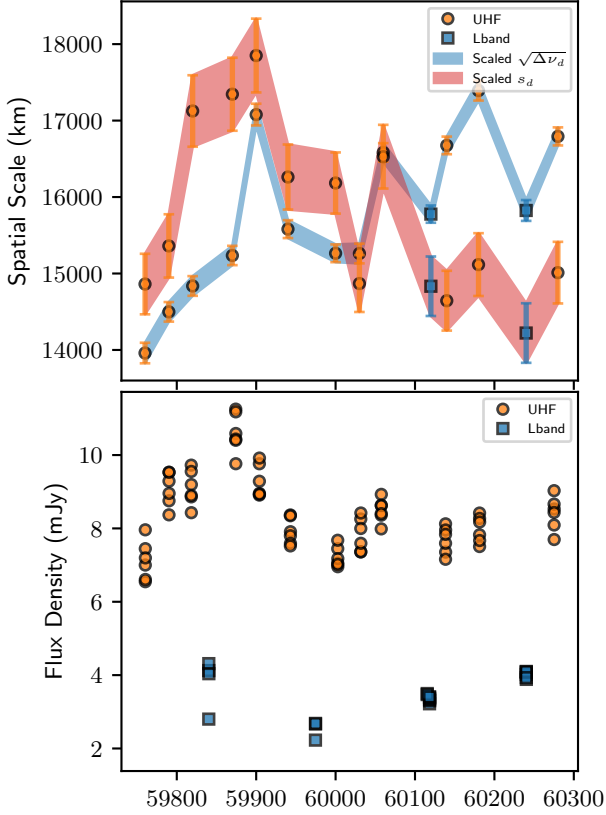


Figure 5. Time series of spatial scale and flux density. The top panel shows the spatial scale variations using two models that depend on the epoch spatial scale (red) and the inferred spatial scale from the scintillation bandwidth measurements (blue), respectively. The middle panel shows the calibrated flux density taken for each observation. Measurements taken at UHF and L-band are shown with circles and squares, respectively. The flux density during late 2022 (MJD 59900) correlated (≈ 0.66) with the spatial scale from our scintillation measurements. The S-band data have not yet been flux-density calibrated.

cascade. The outer scale model describes scattering from discrete objects (‘blobs’ of plasma) along the LoS with sharp boundaries, resulting in the square law distribution. This can be used to describe scattering caused by HII regions, plasma shock fronts at the boundaries of SNRs, and extreme scattering events (Lambert & Rickett 1999, 2000; Coles et al. 2015).

4.2 Anisotropy and IISM Variability

Using the model presented 3.5, we searched for distortions in the scatter-broadened image beyond a simple elliptical scattering disk. These results favour an elliptical anisotropic model, which we use for the rest of our analysis. The effect of this anisotropy on the spatial scale across the orbital phase is shown in Figure 6, for a single UHF observation. The Figure also shows the isotropic model, which is a poor model for the observations. We also searched for higher order perturbations using circular harmonics. The amplitudes of the second and third circular harmonics Δ_2 and Δ_3 were found to be consistent with zero, with amplitudes constrained to be smaller than 3% perturbations of the elliptical image. Therefore, throughout the rest of the manuscript all models use the simpler anisotropic model.

However, future work may find that circular harmonics are necessary to describe stronger, more complex anisotropic scattering screens.

We also searched for epoch-to-epoch variations in the scattering screen properties. This is motivated by the correlated, temporal variations in the spatial scale and flux density as shown in Figure 5. We focused our searches on the parameters that would be most likely affected by epoch-to-epoch variations: namely A_R , ζ , and s_d . We constrained the longitude of the ascending node, Ω , to a Gaussian prior based on measurements and uncertainties derived from our $\Delta\tau_d^{-1}$ model. We also assumed broad Gaussian priors for $V_{\text{IISM},\alpha,\delta}$, centred on our measurements listed in Table 3, with a standard deviation of 20 km s^{-1} . Other parameters were held constant as these were found not to correlate significantly with the aforementioned parameters.

The results from this modelling are presented in Figure 7. We find that most of the parameters of the screen are stable between epochs and consistent with the $\Delta\tau_d^{-1}$ model. The stability of the screen properties across a year is expected to be (and is) seen over longer timescales for other pulsars (Reardon et al. 2020; McKee et al. 2022; Askew et al. 2023). We note that in the third panel of Figure 7, the epochs at MJD ~ 60080 (2023-05-16) and ~ 60212 (2023-09-25) are S-band observations. These epochs were found to have spatial scale measurements greater than the other observations. As we have only two S-band observations, and neither is flux calibrated, it is difficult to determine more information about the sudden rise in spatial scale. Our results are in contrast to Rickett et al. (2014), which reported significant variation in the anisotropy across different epochs. This suggests that we could be observing scattering from a different screen from that modelled in Rickett et al. (2014). We consider this further in Section 5.3.

4.3 Distance Models

We can use the properties of the scattering screen geometry to assess possible values of A_{ISS} and what scattering screen geometries are consistent with published distance estimates to the double pulsar system.

As we cannot calculate A_{ISS} , we treat it as a parameter when assessing possible distances and scattering geometries. Figure 8 shows the posterior distribution for A_{ISS} and D using the V_{ISS} model. The distribution is broad because of the large degeneracy between A_{ISS} and D . To break this degeneracy, previous works have assumed a value for A_{ISS} (Ransom et al. 2004; Shapiro-Albert et al. 2020). In Figure 8, we show four possible values of A_{ISS} published in Lambert & Rickett (1999). For each value, we assume a thin screen at a relative distance consistent with our measurements. For the inner scale model, we assume Kolmogorov turbulence and an inner scale cut-off relative to the spatial scale at a wavenumber of $\kappa_i s_d = 10$. For the outer scale model, we assume $\beta = 4$ and an outer scale cut-off relative to the spatial scale at a wavenumber of $\kappa_o s_d = 10^{-1}$. By using Equation 5 and assumed values for $s = 0.5$, $\Delta\tau_d = 50 \text{ s}$, $\nu = 1.3 \text{ GHz}$, $\Delta\nu_d = 0.2 \text{ MHz}$, and assumed geometries A_{ISS} (which also appear as horizontal lines in Figure 8), we can estimate the distance we might expect. This is shown in the table below.

Assuming one of the distance measurements is correct (i.e., the distance to the double pulsar is $360 \text{ pc} \lesssim D \lesssim 840 \text{ pc}$), we constrain A_{ISS} to be greater than $4.5 \times 10^4 \text{ km s}^{-1}$ and less than $8 \times 10^4 \text{ km s}^{-1}$. Using Table 4 and Figure 8, we can conclude that the timing distance is only consistent with the outer-scale model, and the VLBI distance is consistent with both the outer-scale and Kolmogorov models.

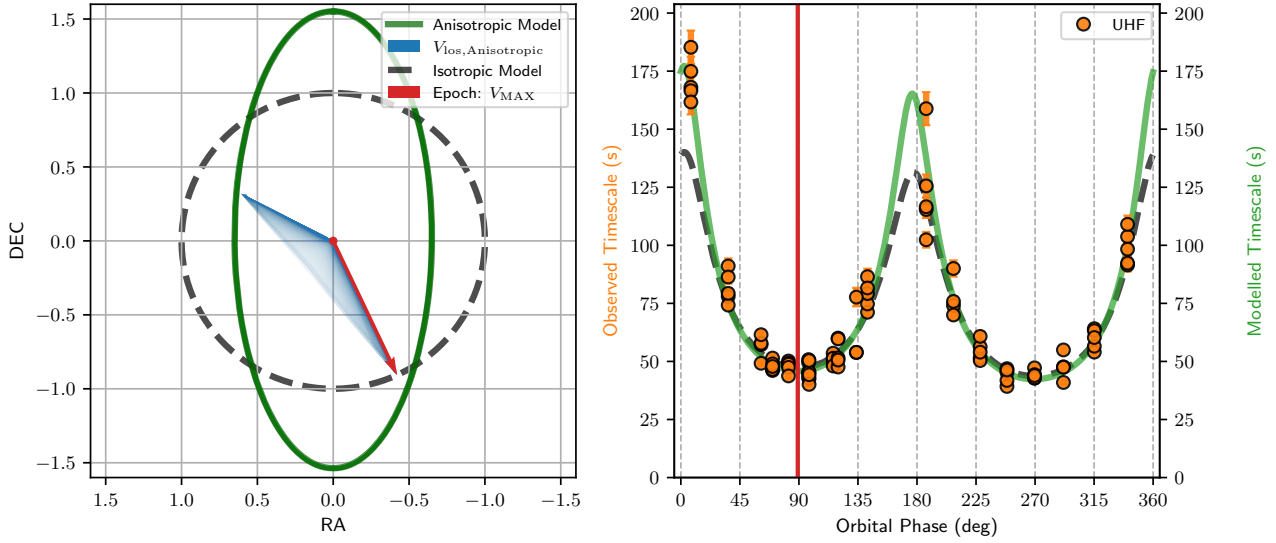


Figure 6. Comparison of models for anisotropic scattering. Left panel: the effective scattered image on the sky. The dashed black line indicates an isotropic scattering image on the sky. The dark green line shows the model using the best-fitting anisotropic model listed in Table 3. The blue lines show the effective velocity (normalised relative to the maximum) at each sample from the model, and the red arrow corresponds to the velocity at the eclipse, where the transverse velocity is maximized. Right panel: Observed timescale measurements, plotted as circles, and the modelled timescale (solid line) shown against the orbital phase. The dashed black line is the same isotropic model from the left panel, and the red vertical line indicates the eclipse. The data and models are derived from the observations on UTC 2023-03-28.

Table 4. Assumed model parameters and geometries leading to distance estimates.

Turbulence Model	A_{ISS} (km s $^{-1}$)	Distance (kpc)
Kolmogorov	4.7×10^4	1.08
Inner-scale model	3.6×10^4	1.83
Outer-scale model	5.6×10^4	0.76
Square-law model	3.1×10^4	2.47

5 DISCUSSION

5.1 Previous scintillation studies of the double pulsar

The double pulsar has been studied using scintillation several times since its discovery (Ransom et al. 2004; Coles et al. 2005; Stinebring et al. 2005; Rickett et al. 2014; Stock & van Kerkwijk 2024), using various approaches and assumptions. Ransom et al. (2004) assumed an isotropic scattering model to infer V_{ISS} . A study of the scattering of radio waves from pulsar A travelling through the magnetosphere of pulsar B by Coles et al. (2005) found that anisotropic scattering ($A_R > 4$) was a better fit for their measured scintillation time scales than an isotropic model. More recently, Rickett et al. (2014) studied the scintillation assuming an anisotropic model. Informed by scintillation timescale measurements, Rickett et al. (2014) used a similar method to our $\Delta\tau_d$ model. These measurements were taken ≈ 17 yr ago, using the Green Bank Telescope. They concluded that the anisotropy varied in both strength and position angle. Interestingly, they inferred a screen at a distance of $s = 0.73 \pm 0.01$. Since then Stock & van Kerkwijk (2024) has re-analysed the results and come to similar conclusions.

Some of our results disagree with those found in Rickett et al. (2014) and Stock & van Kerkwijk (2024). To understand the differences, we have partially re-analysed the data presented in Rickett et al. (2014) using our methodology and code. We measured the fractional

distance of the scattering screen to be $s = 0.70 \pm 0.01$ and the longitude of the ascending node to be $\Omega = 64^\circ \pm 8^\circ$, which is consistent with what they reported. While the uncertainty on s is consistent with their value, the uncertainty on Ω is a factor of four larger, which we attribute to our inclusion of terms to account for excess white noise. Unlike Rickett et al. (2014), we also searched for the longitude of periastron, ω , to check for consistency with the known value from pulsar timing. We compare the results from scintillation to the ω measured in Hu et al. (2022), updated (using the measured rate of periastron advance) to an epoch close to the centre of our MeerKAT data set, $T_0 = 59976.7$ MJD. At this epoch, the longitude of periastron derived from pulsar timing is $\omega = 42.6169^\circ \pm 0.0006^\circ$ and at the reference epoch of the Rickett et al. (2014) data set ($T_0 = 53155.9$ MJD) the longitude derived from pulsar timing is $\omega = 87.0309^\circ \pm 0.0005^\circ$ (Hu et al. 2022). When fitting for ω in our analysis of the MeerKAT data set, we find a consistent value of $\omega = 42.5^\circ \pm 0.2^\circ$. In contrast, when modelling the Rickett et al. (2014) data set, we find $\omega = 310^\circ \pm 30^\circ$, which is inconsistent with pulsar timing at the $3 - \sigma$ level. This suggests our data set and model may be more reliable than those presented in Rickett et al. (2014).

Some of our results disagree with Rickett et al. (2014) and Stock & van Kerkwijk (2024) because of the choice of coordinate systems. We note that the definition of Ω in our analysis is consistent with the definition of Damour & Taylor (1992) and implemented in the scintillation code by Reardon et al. (2019); Reardon (2020). However, the direction of the y-axis (in the plane of the binary orbit, see Figure 2 of Stock & van Kerkwijk 2024) is inverted in Rickett et al. (2014) and Stock & van Kerkwijk (2024) when compared to the Damour & Taylor (1992) definition. This, in addition to the difference we see when measuring ω using Rickett et al. (2014) data, explains the differences we observe when comparing the orbital parameters of i and Ω between Rickett et al. (2014), the timing and our analysis.

We compare our inference on the orbital inclination to that derived using two other independent methods. Firstly, it is also possible to

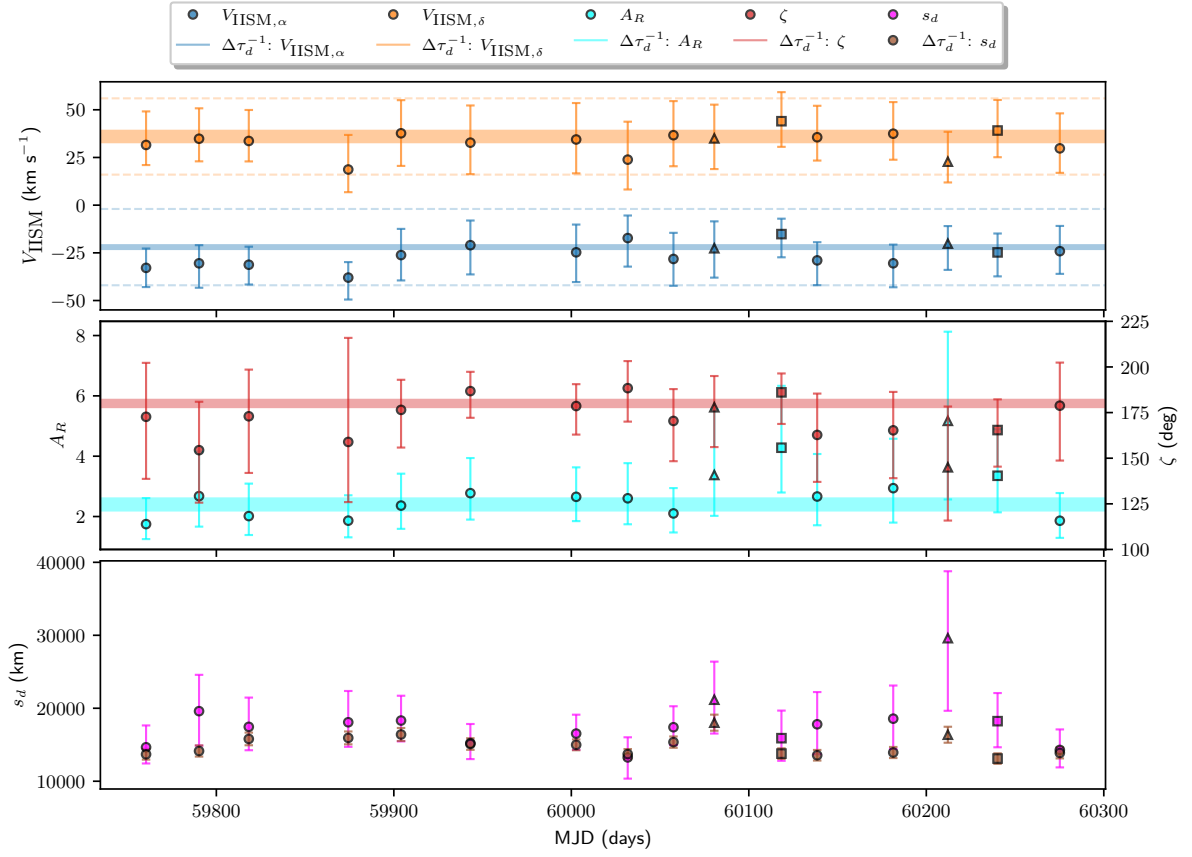


Figure 7. Time series of scattering screen parameters. In each panel, the solid line shows the maximum likelihood parameter values from the $\Delta\tau_d^{-1}$ model. Each data point represents the maximum-likelihood parameters of the epoch-to-epoch model for UHF (circles), L-band (squares), and S-band (triangles). The dashed lines in the top panel show the prior range of the transverse IISM velocity parameters that were used to inform the epoch-to-epoch model. The middle panel shows the axial ratio and anisotropy angle, with scales indicated on the left and right y-axis, respectively.

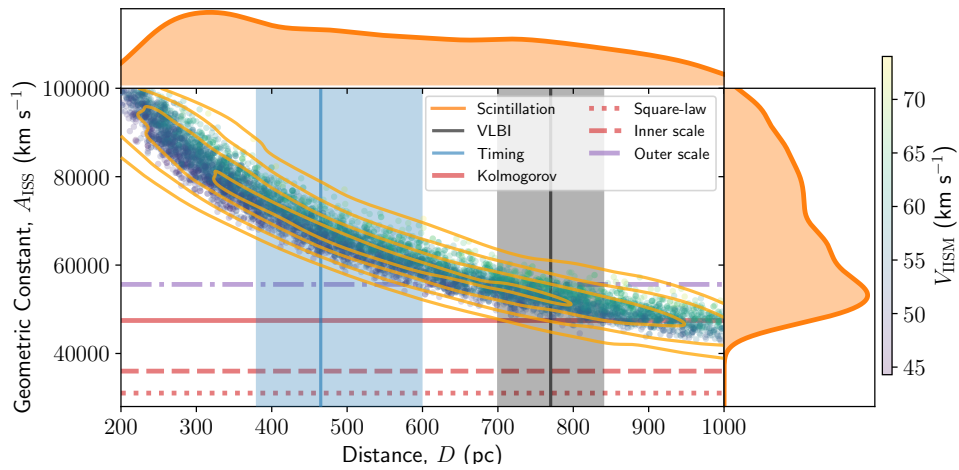


Figure 8. Comparison of plausible distance and scattering geometries for the double pulsar. The orange contours show the $1 - 4\sigma$ confidence levels for the joint posterior distribution of D and A_{ISS} . The vertical lines show the previous distance measurements from the timing (blue) and VLBI parallax (black), with the uncertainties shaded in the same colour to 1σ uncertainty. The horizontal lines show published calculations of A_{ISS} , assuming our inferred relative scattering screen distance. The colour bar represents the magnitude of the transverse scintillation component to the effective velocity.

infer the sense of the inclination angle by modelling the eclipses of pulsar A by pulsar B. Using this method [Lower et al. \(2024\)](#) also found $i > 90^\circ$. Secondly, the analysis of the polarization of the pulsar A pulse profile can be used to infer the system geometry using the rotating vector model ([Radhakrishnan & Cooke 1969](#); [Blaskiewicz et al. 1991](#)) to measure the structure of the beam of pulsar A. Using this model, [Kramer et al. \(2021b\)](#) estimate to be $i = 91.6^\circ \pm 0.1^\circ$.

In our modelling, we use the magnitude of the inclination angle from the timing model of [Kramer et al. \(2021a\)](#) as a prior. Our results support $i > 90^\circ$ (see Table 3) with a log BF ≈ 21 . This is therefore consistent with recent studies that find $i > 90^\circ$ [Kramer et al. \(2021b\)](#); [Hu et al. \(2022\)](#) and [Lower et al. \(2024\)](#) and inconsistent with [Ransom et al. \(2004\)](#) and [Rickett et al. \(2014\)](#).

Our model of the relative screen distance (see Table 3) is in strong tension with the results of [Rickett et al. \(2014\)](#). Given the difference between these observations (~ 17 yr), if a single screen was responsible for all of the observed scintillation, it would need to be at least $\mathcal{O}(100)$ AU in projected transverse extent. Multiple scattering screens along the LoS are not uncommon ([Mall et al. 2022](#); [Ocker et al. 2024](#); [Reardon et al. 2024a](#)). These can often appear as scintillation arcs ([Stinebring et al. 2001](#)) with different curvature values from distinct parabolic arcs in the secondary spectrum (the two dimensional spectrum of the dynamic spectrum). It is also not unlikely that the scattering screens can vary over \sim decades of observations ([Walker et al. 2022](#)). Therefore, we conclude that we are probing a different area of the IISM along the LoS.

It is also possible to use the secondary spectrum to characterise the ISM and orbital dynamics of pulsars. Indeed, previous work has also investigated the secondary spectrum in scintillation towards the double pulsar in [Stinebring et al. \(2005\)](#). The utility of using parabolic arcs depends on the sharpness of the arcs. At lower frequencies (UHF) the scintillation arcs are diffuse due to the relatively high strength of scattering and only modest anisotropy. Therefore, [Stinebring et al. \(2005\)](#) conclude that observations at higher frequencies and with a greater signal-to-noise ratio would yield more promising results. Our results agree. Work analysing the secondary spectrum of GBT and MeerKAT data is ongoing (D. Montalvo et al., in prep.).

5.2 Distance to the double pulsar system

Systematic errors may be impacting published distance measurements to pulsars ([Verbiest et al. 2012](#); [Ding et al. 2023](#)). Some of the errors that impact pulsar timing include DM variations and intrinsic spin noise, which can be modelled ([Keith et al. 2013](#)), and mitigated ([Goncharov et al. 2021](#)). The high ecliptic latitude ($b = -51.2^\circ$) of the double pulsar system reduces the impact of the solar wind on DM variations but increases systematic errors and reduces the precision of a distance measurement ([Kramer et al. 2021a](#)).

The measurement of a trigonometric parallax through VLBI can potentially be affected by refractive image wander caused by the turbulent IISM and the ionosphere of the Earth. These effects in the current analysis of the double pulsar are negligible, however, this may change in the future, and other pulsars could benefit from a detailed understanding of the scattering ([Kramer et al. 2021a](#)). Refractive image wander can be caused by phase gradients in the IISM, which have been seen to change across the orbital and annual phase of the double pulsar ([Rickett et al. 2014](#)). The strength of refractive image wander can be characterised by a refraction angle θ_r . The refractive scintillation for the double pulsar has a characteristic timescale on the order of months (discussed below). As the Very Long Baseline Array (the instrument used for VLBI observations of the double pulsar) is in the northern hemisphere (and the double pulsar is in the southern

sky), the array also has to point close to the horizon, potentially adding to the systematic uncertainty. This is because the antennas in the array have to observe through large columns of the atmosphere and ionosphere of the Earth, impacting array calibration.

Our scintillation analysis can be used to critically examine the pulsar timing and VLBI-inferred distance measurements. We can compare our estimate of refractive image wander to that previously inferred from DM variations. We estimate the image wander from variations in the spatial scale. We can attribute the variations in spatial scale to refractive effects because of the significant correlation between flux density variations and spatial scale. We first estimate the Fresnel scale, $r_f = \sqrt{D_s/k}$, where $k = 2\pi/\lambda$ is the wavenumber. We then calculate the strength of scattering, $u = r_f/s_d$, using the epoch-by-epoch spatial scale measurements. Assuming Kolmogorov turbulence, the diffractive scattering angle and refractive image wander are $\theta_d = 2\sqrt{2} \log 2 \lambda / (\pi s_d)$ and $\theta_r = \theta_d u^{-1/3}$, respectively ([Rickett 1990](#)). In our observations, we find the RMS for θ_r to be ≈ 0.825 mas at 1 GHz.

This is notably larger than what was estimated by [Kramer et al. \(2021a\)](#). From DM variations, they estimated the RMS variations in θ_r to be 0.177 mas, at a reference frequency of 1.56 GHz. However, the peak-to-peak variations in image wander were found to be as large as 0.8 mas. Our RMS $\theta_r \approx 0.339$ mas is much larger when scaled to this frequency, assuming $\theta_r \propto \nu^{-2}$. The differences are not surprising. Approximately 3 yr passed between the last of their measurements and the first of ours. Alternatively, it could be the case that the ISM anisotropy is more pronounced in directions perpendicular to the pulsar proper motion, as we infer. In this case, the effects of image wander would have been underestimated by [Kramer et al. \(2021a\)](#). If refractive image wander had annual or semi-annual variations, it could impact VLBI and pulsar timing measurements.

Earlier in Section 4.3, we introduced how a third independent distance measurement could potentially resolve tension between the timing and VLBI distances. Here we determined that only the Kolmogorov and outer-scale models are consistent with this distance. The frequency dependence of the scintillation bandwidth suggests the turbulence is not purely Kolmogorov. A Kolmogorov model with an inner-scale or outer-scale component (different from those plotted in Figure 8) may describe the structure of the medium. A similar argument can be applied to a square law medium with a different outer scale component. Further support for the VLBI distance comes from the association of the scattering screen with the Gum Nebula, which we discuss in the next section.

5.3 Screen associations

We next explore the possibility and implications of the observed scattering screen being associated with the Gum Nebula. The Gum Nebula has several different speculated formation channels, including a supernova explosion, an HII region, a wind-blown bubble, or possibly a combination thereof ([Reynolds 1976a,b](#); [Woermann et al. 2001](#); [Sushch et al. 2011](#); [Purcell et al. 2015](#)). The most common explanation is that it is a SNR resultant from a supernova explosion occurring approximately 1 Myr ago ([Reynolds 1976a,b](#)). To investigate the progenitor of the nebula, [Woermann et al. \(2001\)](#) modelled the peculiar velocity of the runaway star ζ Puppis, which is thought to have gained its high velocity due to a kick after the supernova explosion of a binary companion. They found that its path crosses the modelled centre of the asymmetric expansion of the neutral gas ([Reynolds 1976b](#); [Woermann et al. 2001](#)). Assuming this scenario is correct, [Woermann et al. \(2001\)](#) date the age of supernova to be

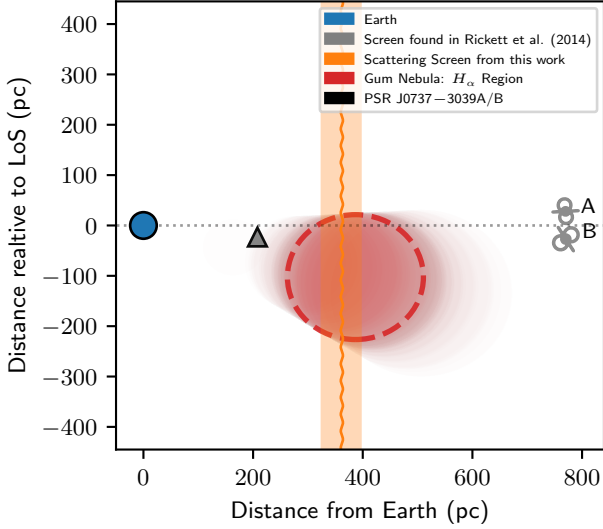


Figure 9. Model of the line of sight to the double pulsar. From left to right we show the Earth, the screen position measured by Rickett et al. (2014) (grey marker), our screen position (orange line), the Gum Nebula at a distance of 400 ± 60 pc, with an inferred radius of 124 pc at this distance (dashed red line) (Sushch et al. 2011; Purcell et al. 2015; O’Neill et al. 2024), and the double pulsar J0737–3039A/B assuming the VLBI distance of 770 pc. The transparent red circles are random draws are taken from the possible distance to the nebula, to show distance uncertainty.

1.5 Myr ago. For the subsequent analysis and text, we also assume the progenitor of the Gum Nebula is a SNR.

Estimations of the age of the supernova depend on the properties of the explosion and the ambient interstellar medium. Using the dynamics of SNRs, Cioffi et al. (1988) estimated the ambient density of the IISM, n_o , that a SNR “ploughed through” to form what we observe today. Estimations from Reynolds (1976b) estimated this to be as low as $n_o \sim 0.1 - 0.2 \text{ cm}^{-3}$. More recently Purcell et al. (2015) estimated it to be $0.2 < n_o < 0.9 \text{ cm}^{-3}$. Sushch et al. (2011) estimated $n_o = 0.07 \text{ cm}^{-3}$, assuming an age of supernova 1.5 Myr, kinetic energy of supernova explosion $E_{51} = 10^{51}$ erg, a distance to the Gum Nebula of 400 pc and relative solar metallicity $\zeta_m = 1$. The expansion velocity of the ionized gas, V_s , will also affect this inference, which was originally estimated to be $10\text{--}30 \text{ km s}^{-1}$ (Reynolds 1976a).

Recent work has modelled the Gum Nebula and local ionized gas regions, including the Vela supernova remnant and local bubble (Sushch et al. 2011; O’Neill et al. 2024). To simplify the model of the $H\alpha$ region, we assume a sphere at a distance of 400 ± 60 pc with a radius of 124 pc (Sushch et al. 2011; O’Neill et al. 2024). Figure 9 shows a schematic representation of the LoS to the double pulsar, including the locations of the pulsar, the scattering screen, and the Gum Nebula. The screen grazes the edge of the nebula. The graphic also shows the position of the scattering screen measured by Rickett et al. (2014).

An $H\alpha$ image of the ionized gas associated with the direction of the Gum Nebula is shown in Figure 1 from observations from the Southern $H\alpha$ Sky Survey Atlas (Gaustad et al. 2001). The $H\alpha$ region is also represented in Figure 9, showing the overlap with the LoS to the double pulsar. This indicates that, when assuming the VLBI distance to the double pulsar, our scattering screen is likely associated with the Gum Nebula. The screen is therefore expected to be at a distance consistent with the outer edge of the nebula ($D_s = 360^{+30}_{-40}$ pc). It also

Table 5. Comparison of ISM models and pulsar distance measurements. An outer-scale scattering screen originating in the Gum Nebula and a VLBI distance to the double pulsar are the most consistent with our observations.

Turbulence Model	Timing distance	VLBI distance
Kolmogorov	×	✓
Outer-scale model	✓	✓
Inner-scale model	×	×
Square-law model	×	×
Gum Nebula	×	✓

suggests the distribution of material with the scattering screen is consistent having density fluctuations following an outer-scale model.

We summarise evidence supporting plausible scattering screen models and distances in Table 5. If we assume the distance inferred from pulsar timing, the screen would be located at a distance $D_s = 220 \pm 30$ pc from Earth so it would not be associated with the Gum Nebula. Thus, the association of the scattering screen with the Gum Nebula provides additional support for the VLBI distance and an outer-scale model for the turbulence. Throughout the remainder of the text, we assume the VLBI distance to the double pulsar for our analysis.

5.4 Applications of SNR association

Using scattering screen velocities, it is possible to measure the expansion velocity, V_s , of the SNR. This method assumes that the scattering screen is at the edge of a SNR where V_s is the projected velocity given the measured transverse velocity V_{IISM} . To calculate this, we used a vector from the centre of the Gum Nebula and used our measurement of the screen velocity V_{IISM} to determine V_s .

The expansion of a SNR occurs in different stages (Woltjer 1972; Cioffi et al. 1988), beginning with the Sedov-Taylor (ST) stage (Taylor 1950; Sedov 1959). When the gas cools, a supernova remnant shell is formed at a time

$$t_{\text{sf}} = 3.61 \times 10^4 \frac{E_{51}^{3/14}}{\zeta_m^{5/14} n_o^{4/7}}, \quad (14)$$

where E_{51} is the kinetic energy of the supernova explosion in units of 10^{51} erg, ζ_m is the metallicity (measured relative to solar metallicity) that the shell “snowploughs” through the ambient IISM, of which the ambient density is n_o and expressed in units of cm^{-3} (Cioffi et al. 1988). The time at the end of the ST stage and the beginning of the pressure-driven snowplough (PDS) stage is given by $t_{\text{PDS}} = t_{\text{sf}}/e$, where e is Euler’s number. We can then determine the age of a supernova t using the normalised relative time $t_* = t/t_{\text{PDS}}$ (Cioffi et al. 1988):

$$t = 1.33 \times 10^4 \frac{t_* E_{51}^{3/14}}{\zeta_m^{5/14} n_o^{4/7}} \text{ yr}. \quad (15)$$

In the late stage of expansion of a SNR, the velocity and radius of expansion can be modelled as

$$\begin{aligned} v_s &= 413 n_o^{1/7} \zeta_m^{3/14} E_{51}^{1/14} \left(\frac{4}{3} t_* - \frac{1}{3} \right)^{-7/10} \\ &= v_{\text{PDS}} \left(\frac{4}{3} t_* - \frac{1}{3} \right)^{-7/10} \text{ km s}^{-1}, \end{aligned} \quad (16)$$

and,

$$\begin{aligned} R_s &= 14 \frac{E_{51}^{2/7}}{\zeta_m^{1/7} n_o^{3/7}} \left(\frac{4}{3} t_* - \frac{1}{3} \right)^{3/10} \\ &= R_{\text{PDS}} \left(\frac{4}{3} t_* - \frac{1}{3} \right)^{3/10} \text{ pc}, \end{aligned} \quad (17)$$

respectively (Cioffi et al. 1988).

Using these relationships we can express t_* in terms of R_s , V_s , and t ,

$$t_* = \left[4 - 1.18 \times 10^6 \frac{R_s}{V_s t} \right]^{-1}, \quad (18)$$

and then rearrange to solve for E_{51} and n_o in terms of R_s , V_s , ζ_m , and t ,

$$E_{51} = \frac{R_s^2}{14} \frac{V_s^6}{413} \zeta_m^{-1} \left(\frac{4}{3} t_* - \frac{1}{3} \right)^{18/5}, \quad (19)$$

$$n_o = \frac{R_s^{-1}}{14} \frac{V_s^4}{413} \zeta_m^{-1} \left(\frac{4}{3} t_* - \frac{1}{3} \right)^{31/10}, \quad (20)$$

which allows us to directly measure the energy of a supernova explosion and the ambient density of the IISM it passes through.

In Figure 1, we show the projected transverse velocity of the screen on the sky, $V_{\text{scr}} = 29 \pm 4 \text{ km s}^{-1}$. Here, we have accounted for the differential rotation of the Galaxy at the screen location, based on code used in Shamohammadi et al. (2024). The direction of motion is only modestly askew from a radial direction from the purported centre of the nebula. This could be caused by asymmetries in the ionized gas expanding into the ambient IISM if the screen is associated with the Gum Nebula.

In this case, the expansion rate of the ionized gas would be $V_s = 35 \pm 5 \text{ km s}^{-1}$. As far as we are aware, this is the first time an expansion rate has been measured this way. The expansion velocity of the ionised gas we measure is significantly larger than that expected for a HII region which is thought to be ($\sim 4 \text{ km s}^{-1}$, Lasker 1966). However, this value is consistent with the lower limit of the SNR expansion provided in Sridharan (1992) and Woermann et al. (2000) of $V_s = 12 \text{ km s}^{-1}$ and close to the initial estimates of 10–30 km s^{-1} (Reynolds 1976a).

Our inferred velocity is also a factor of a few larger than the expected mean of the (turbulent) plasma velocity in the IISM $|V_{\text{IISM}}| = 10 \text{ km s}^{-1}$ (Goldreich & Sridhar 1995). This suggests that there are shocks in the ionized shell of the Gum Nebula, resulting in gas travelling at supersonic speeds, or that the shell is associated with a blast wave such as from a supernova explosion. While towards some pulsars, screen velocities (Sprenger et al. 2022; Mall et al. 2022; Liu et al. 2023; Wu et al. 2024) are lower and consistent with thermal velocity, several works find screen velocities significantly greater than the mean plasma velocity (Reardon et al. 2020; McKee et al. 2022; Walker et al. 2022; Askew et al. 2023; Reardon et al. 2024a), like our measurements.

We applied these results to the dynamics of SNR using equations 14–20. We used our estimates of V_s and R_s and their 1σ uncertainties. We limit the possible values for E_{51} , n_o , and t to physical ranges of 10^{50} to 10^{52} erg, 0.01 to 1 cm^{-3} , and 0.5 to 3.2 Myr , respectively. The results can be visualised in the one- and two-dimensional marginal posterior distributions shown in Figure 10.

Using these solutions to the Equations 14–20, we find that the degree of metallicity has a negligible impact on the results, as expected. Additionally, if we use the published estimates for n_o (Purcell et al. 2015), we find these results are consistent with a supernova that is

a few times more energetic than previously predicted. We measure the age of the supernova to be $t = 1.1 \pm 0.1 \text{ Myr}$. An expected age of the SNR of $t \approx 1 \text{ Myr}$ is consistent with Reynolds (1976b) given our expansion velocity and radius of the Gum Nebula. Our estimate of the age of the supernova means the association with ζ Puppis with the formation of the Gum Nebula is less likely.

6 CONCLUSIONS

The double pulsar has significantly advanced several aspects of fundamental physics. These tests have been made possible because of a concentrated effort to understand and model the times of arrival from both pulsars A and B. One of these tests is the measurement of the orbital decay due to gravitational wave emission. Much like the Hulse-Taylor binary (Hulse & Taylor 1975), an accurate measurement of the distance is essential for this test and future precise tests of GR (Kramer et al. 2021a; Hu et al. 2022).

We have developed a model of the scintillation, exploring its frequency dependence and measuring its spatial scale. We find that the observed scintillation is consistent with originating in a single dominant anisotropic scattering screen located at the edge of the Gum nebula. We have constrained the sense of the inclination angle of and measured the longitude of the ascending node of the orbit.

To accomplish this, we considered several possible models for the IISM and effects that could impact our analysis of diffractive scintillation patterns. Our data supports a scattering screen with an outer scale. Such screens are expected to be observed towards HII regions or collections of plasma with steep edges, such as SNRs like the Gum Nebula.

While exploring possible associations along the LoS, we discovered that the scattering screen grazes the edge of the Gum Nebula H α emission. We have measured the expansion of the ionized gas of the Gum Nebula to be $V_s = 35 \pm 5 \text{ km s}^{-1}$. This was used to estimate the properties of the SNR, including the ambient density of the IISM the SNR ploughed through, the energy of the supernova explosion, and the relative solar metallicity of the ambient IISM. In a novel way, using scintillation, we place limits on these physical properties of the IISM and find the age of the SNR to be $t \approx 1 \text{ Myr}$.

Any apparent tension between the pulsar timing and VLBI parallax distance can be solved by introducing a third independent measurement. Using scintillation, we have provided independent support that VLBI measurements provide a more reliable distance to the double pulsar than those presently achieved through pulsar timing. In the future it might be possible to use scintillation to make an independent distance measurement with improved theoretical modelling of the relationship between scintillation time scales, bandwidths, and velocities.

Future work may determine A_{ISS} when scintillation shows relatively weaker chromaticity, like we have observed. This will allow for independent distance measurements to sources like the double pulsar.

If the distance is well constrained, scintillation observations can be used to test models of the IISM structure and to probe the properties of intervening objects along the line of sight. Pulsars that are good targets for such a study are the binary millisecond pulsars PSRs J0437–4715, J1614–2230, J1643–1224, or J2222–0137 (Guo et al. 2021; Mall et al. 2022; Shamohammadi et al. 2024; Reardon et al. 2024b). This would help us develop an understanding of our Galaxy and the fundamental properties of scattering, which can impact precision pulsar timing. However, if the distance is unknown and theory is developed to determine A_{ISS} for a wider range of sightlines,

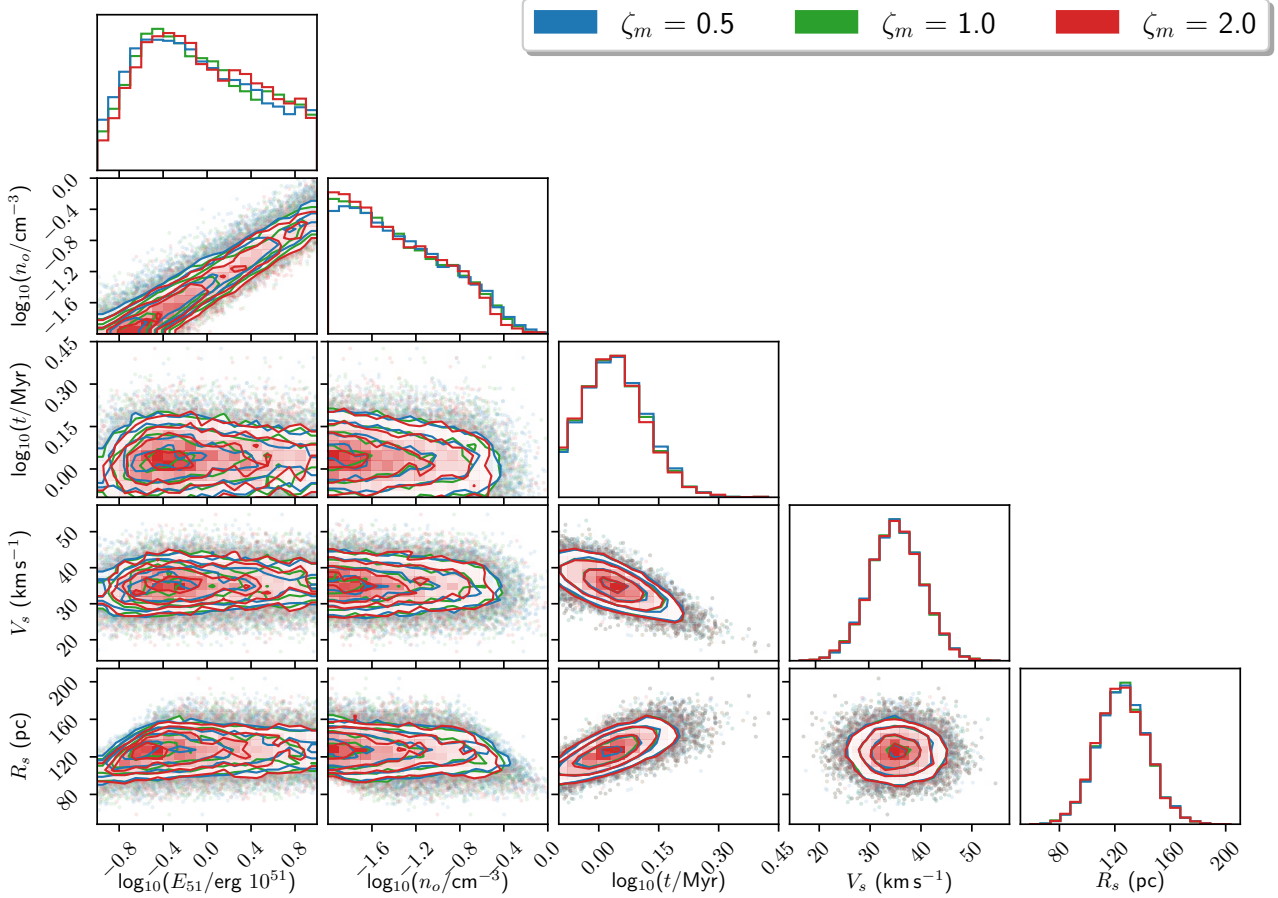


Figure 10. Two-dimensional posterior distributions for supernova scenario. Different metallicities (measured relative to solar metallicity) are shown in blue ($\zeta_m = 0.5$), green ($\zeta_m = 1.0$), and red ($\zeta_m = 2.0$). The normalised one-dimensional distributions appear to be weakly dependent on ζ_m .

a detailed study using scintillation could provide an independent measurement of distance for pulsars that show pronounced scintillation in the decimeter wavelength range, such as PSRs J0613–0200, J0614–3329, or J1757–5322 (Gütika et al. 2023; Shamohammadi et al. 2024). Appendix A presents a generalised method of determining the distances to pulsars using scintillation.

The double pulsar system will continue to provide improved tests of general relativity. When it precesses back into the line of sight, scintillometry of the B-pulsar may be possible with the improved sensitivity of MeerKAT or the Square Kilometre Array.

ACKNOWLEDGEMENTS

We thank the referee for their valuable feedback, which has improved the structure and quality of the manuscript. We acknowledge the Wurundjeri People, the traditional owners of the land on which Swinburne University of Technology (Hawthorn) is located. This work was performed on the OzSTAR national facility at Swinburne University of Technology. The OzSTAR program receives funding in part from the Astronomy National Collaborative Research Infrastructure Strategy (NCRIS) allocation provided by the Australian Government, and from the Victorian Higher Education State Investment Fund (VHE-SIF) provided by the Victorian Government. The MeerKAT telescope is operated by the South African Radio Astronomy Observatory (SARAO), which is a facility of the National Research Foundation,

an agency of the Department of Science and Innovation. SARAO acknowledges the ongoing advice and calibration of GPS systems by the National Metrology Institute of South Africa (NMISA) and the time space reference systems department of the Paris Observatory. PTUSE was developed with support from the Australian SKA Office and Swinburne University of Technology. Parts of this work were funded through the ARC Centre of Excellence for Gravitational Wave Discovery (CE170100004 and CE230100016). RMS acknowledges support through ARC Future Fellowship FT190100155. This work is supported by the Max-Planck Society as part of the ‘LEGACY’ collaboration with the Chinese Academy of Sciences on low-frequency gravitational wave astronomy. This research has made use of NASA’s Astrophysics Data System and software packages, including: MATPLOTLIB (Hunter 2007), SCIPY (Virtanen et al. 2020), ASTROPY (Collaboration et al. 2022), NUMPY (Harris et al. 2020), BILBY (Ashton et al. 2019).

DATA AVAILABILITY

Data and data products are available upon reasonable request to the corresponding author.

REFERENCES

- Anderson T. W., Darling D. A., 1954, *Journal of the American Statistical Association*, 49, 765
- Antoniadis J., et al., 2013, *Science*, 340, 448
- Antoniadis J., Tauris T. M., Ozel F., Barr E., Champion D. J., Freire P. C. C., 2016, *arXiv e-prints*, p. [arXiv:1605.01665](#)
- Armstrong J. W., Rickett B. J., Spangler S. R., 1995, *ApJ*, 443, 209
- Ashton G., et al., 2019, *Astrophys. J. Suppl.*, 241, 27
- Askew J., Reardon D. J., Shannon R. M., 2023, *MNRAS*, 519, 5086
- Bailes M., et al., 2020, *Publ. Astron. Soc. Australia*, 37, e028
- Bhat N. D. R., Gupta Y., Rao A. P., 1998, *ApJ*, 500, 262
- Bhat N. D. R., Cordes J. M., Camilo F., Nice D. J., Lorimer D. R., 2004, *ApJ*, 605, 759
- Blaskiewicz M., Cordes J. M., Wasserman I., 1991, *ApJ*, 370, 643
- Breton R. P., 2009, PhD thesis, McGill University, Canada
- Camilo F., Foster R. S., Wolszczan A., 1994, *ApJ*, 437, L39
- Chandran B. D. G., Backer D. C., 2002, *ApJ*, 576, 176
- Cioffi D. F., McKee C. F., Bertschinger E., 1988, *ApJ*, 334, 252
- Coles W. A., Frehlich R. G., Rickett B. J., Codona J. L., 1987, *ApJ*, 315, 666
- Coles W. A., McLaughlin M. A., Rickett B. J., Lyne A. G., Bhat N. D. R., 2005, *The Astrophysical Journal*, 623, 392–397
- Coles W. A., et al., 2015, *ApJ*, 808, 113
- Collaboration T. A., et al., 2022, *The Astrophysical Journal*, 935, 167
- Cordes J. M., 1986, *ApJ*, 311, 183
- Cordes J. M., Rickett B. J., 1998, *The Astrophysical Journal*, 507, 846
- Cordes J. M., Pidwerbetsky A., Lovelace R. V. E., 1986, *ApJ*, 310, 737
- Cromartie H. T., et al., 2020, *Nature Astronomy*, 4, 72
- Damour T., Taylor J. H., 1992, *Phys. Rev. D*, 45, 1840
- Desai K. M., Fey A. L., 2001, *ApJS*, 133, 395
- Ding H., et al., 2023, *MNRAS*, 519, 4982
- Florinski V., Balsara D. S., Bhoriya D., Zank G. P., Biswas S., Sharma S., Subramanian S., 2024, *arXiv e-prints*, p. [arXiv:2410.22589](#)
- Gaustad J. E., McCullough P. R., Rosing W., Van Buren D., 2001, *PASP*, 113, 1326
- Gitika P., et al., 2023, *MNRAS*, 526, 3370
- Goldreich P., Sridhar S., 1995, *ApJ*, 438, 763
- Goncharov B., et al., 2021, *ApJ*, 917, L19
- Gum C. S., 1952, *The Observatory*, 72, 151
- Guo Y. J., et al., 2021, *A&A*, 654, A16
- Gupta Y., Rickett B. J., Lyne A. G., 1994, *MNRAS*, 269, 1035
- Gwinn C. R., Taylor J. H., Weisberg J. M., Rawley L. A., 1986, *AJ*, 91, 338
- Harris C. R., et al., 2020, *Nature*, 585, 357
- Hotan A. W., van Straten W., Manchester R. N., 2004, *Publ. Astron. Soc. Australia*, 21, 302
- Hu H., Freire P. C. C., 2024, *Universe*, 10, 160
- Hu H., Kramer M., Wex N., Champion D. J., Kehl M. S., 2020, *MNRAS*, 497, 3118
- Hu H., et al., 2022, *A&A*, 667, A149
- Hulse R. A., Taylor J. H., 1975, *ApJ*, 195, L51
- Hunter J. D., 2007, *Computing in Science & Engineering*, 9, 90
- Jonas J., MeerKAT Team 2016, in MeerKAT Science: On the Pathway to the SKA. p. 1, [doi:10.22323/1.277.0001](#)
- Jow D. L., Pen U.-L., Baker D., 2024, *MNRAS*, 528, 6292
- Kaspi V. M., Taylor J. H., Ryba M. F., 1994, *ApJ*, 428, 713
- Keith M. J., et al., 2013, *MNRAS*, 429, 2161
- Kramer M., et al., 2005, in Rasio F. A., Stairs I. H., eds, *Astronomical Society of the Pacific Conference Series Vol. 328, Binary Radio Pulsars*. p. 59 ([arXiv:astro-ph/0405179](#)), [doi:10.48550/arXiv.astro-ph/0405179](#)
- Kramer M., et al., 2006, *Science*, 314, 97
- Kramer M., et al., 2021a, *Physical Review X*, 11, 041050
- Kramer M., et al., 2021b, *MNRAS*, 504, 2094
- Krishnakumar M. A., Maan Y., Joshi B. C., Manoharan P. K., 2019, *ApJ*, 878, 130
- Lambert H. C., Rickett B. J., 1999, *ApJ*, 517, 299
- Lambert H. C., Rickett B. J., 2000, *ApJ*, 531, 883
- Lasker B. M., 1966, *ApJ*, 143, 700
- Lattimer J. M., 2021, *Annual Review of Nuclear and Particle Science*, 71, 433
- Lattimer J. M., Prakash M., 2004, *Science*, 304, 536
- Liu Y., et al., 2023, *Science China Physics, Mechanics, and Astronomy*, 66, 119512
- Lower M. E., et al., 2024, *A&A*, 682, A26
- Lutz T. E., Kelker D. H., 1973, *PASP*, 85, 573
- Lyne A. G., et al., 2004, *Science*, 303, 1153
- Lyutikov M., Thompson C., 2005, *ApJ*, 634, 1223
- Main R., Lin R., van Kerkwijk M. H., Pen U.-L., Rudnitskii A. G., Popov M. V., Soglasnov V. A., Lyutikov M., 2021, *ApJ*, 915, 65
- Mall G., et al., 2022, *MNRAS*, 511, 1104
- McKee J. W., Zhu H., Stinebring D. R., Cordes J. M., 2022, *ApJ*, 927, 99
- Miles M. T., et al., 2023, *MNRAS*, 519, 3976
- Miles M. T., et al., 2025, *MNRAS*, 536, 1489
- Noutsos A., et al., 2020, *A&A*, 643, A143
- O'Neill T. J., Zucker C., Goodman A. A., Edenhofer G., 2024, *arXiv e-prints*, p. [arXiv:2403.04961](#)
- Ocker S. K., et al., 2024, *MNRAS*, 527, 7568
- Ord S. M., Bailes M., van Straten W., 2002, *ApJ*, 574, L75
- Pagani L., Lefèvre C., Bacmann A., Steinacker J., 2012, *A&A*, 541, A154
- Pen U.-L., King L., 2012, *MNRAS*, 421, L132
- Perera B. B. P., Lomiashvili D., Gourgouliatos K. N., McLaughlin M. A., Lyutikov M., 2012, *ApJ*, 750, 130
- Purcell C. R., et al., 2015, *ApJ*, 804, 22
- Radhakrishnan V., Cooke D. J., 1969, *Astrophys. Lett.*, 3, 225
- Ransom S. M., Kaspi V. M., Ramachandran R., Demorest P., Backer D. C., Pfahl E. D., Ghigo F. D., Kaplan D. L., 2004, *ApJ*, 609, L71
- Reardon D. J., 2020, *Scintools: Pulsar scintillation data tools*, *Astrophysics Source Code Library*, record ascl:2011.019 ([ascl:2011.019](#))
- Reardon D. J., Coles W. A., 2023, *MNRAS*, 521, 6392
- Reardon D. J., Coles W. A., Hobbs G., Ord S., Kerr M., Bailes M., Bhat N. D. R., Venkatraman Krishnan V., 2019, *MNRAS*, 485, 4389
- Reardon D. J., et al., 2020, *ApJ*, 904, 104
- Reardon D. J., et al., 2024a, *arXiv e-prints*, p. [arXiv:2410.21390](#)
- Reardon D. J., et al., 2024b, *ApJ*, 971, L18
- Reynolds R. J., 1976a, *ApJ*, 203, 151
- Reynolds R. J., 1976b, *ApJ*, 206, 679
- Rickett B. J., 1977, *ARA&A*, 15, 479
- Rickett B. J., 1990, *Annual Rev. Astron. Astrophys.*, 28, 561
- Rickett B. J., Lyne A. G., 1968, *Nature*, 218, 934
- Rickett B. J., et al., 2014, *ApJ*, 787, 161
- Riley J., et al., 2022, *ApJS*, 258, 34
- Sedov L. I., 1959, *Similarity and Dimensional Methods in Mechanics*. Elsevier Inc, [doi:https://doi.org/10.1016/C2013-0-08173-X](#)
- Serylak M., et al., 2021, *MNRAS*, 505, 4483
- Shamohammadi M., et al., 2023, *MNRAS*, 520, 1789
- Shamohammadi M., et al., 2024, *MNRAS*, 530, 287
- Shannon R. M., Cordes J. M., 2017, *MNRAS*, 464, 2075
- Shapiro I. I., 1964, *Phys. Rev. Lett.*, 13, 789
- Shapiro-Albert B. J., McLaughlin M. A., Lam M. T., Cordes J. M., Swiggum J. K., 2020, *ApJ*, 890, 123
- Shklovskii I. S., 1970, *Soviet Ast.*, 13, 562
- Spiewak R., et al., 2022, *Publ. Astron. Soc. Australia*, 39, e027
- Sprenger T., Main R., Wucknitz O., Mall G., Wu J., 2022, *MNRAS*, 515, 6198
- Sridharan T. K., 1992, *Journal of Astrophysics and Astronomy*, 13, 217
- Stairs I. H., Thorsett S. E., Dewey R. J., Kramer M., McPhee C. A., 2006, *MNRAS*, 373, L50
- Stinebring D. R., McLaughlin M. A., Cordes J. M., Becker K. M., Goodman J. E. E., Kramer M. A., Sheard J. L., Smith C. T., 2001, *ApJ*, 549, L97
- Stinebring D. R., Hill A. S., Ransom S. M., 2005, in Rasio F. A., Stairs I. H., eds, *Astronomical Society of the Pacific Conference Series Vol. 328, Binary Radio Pulsars*. p. 349
- Stinebring D. R., et al., 2022, *arXiv e-prints*, p. [arXiv:2207.08756](#)
- Stock A. M., van Kerkwijk M. H., 2024, *arXiv e-prints*, p. [arXiv:2407.16876](#)
- Sushch I., Hnatyk B., Neronov A., 2011, *A&A*, 525, A154
- Sutton J. M., 1971, *MNRAS*, 155, 51

- Tauris T. M., et al., 2017, *ApJ*, **846**, 170
- Taylor G., 1950, *Proceedings of the Royal Society of London Series A*, **201**, 159
- Verbiest J. P. W., Weisberg J. M., Chael A. A., Lee K. J., Lorimer D. R., 2012, *ApJ*, **755**, 39
- Virtanen P., et al., 2020, *Nature Methods*, **17**, 261
- Walker M. A., Tuntsov A. V., Bignall H., Reynolds C., Bannister K. W., Johnston S., Stevens J., Ravi V., 2017, *ApJ*, **843**, 15
- Walker K., Reardon D. J., Thrane E., Smith R., 2022, *ApJ*, **933**, 16
- Wang R., et al., 2025, *Science China Physics, Mechanics, and Astronomy*, **68**, 239512
- Woermann B., Gaylard M. J., Otrupcek R., 2000, *MNRAS*, **315**, 241
- Woermann B., Gaylard M. J., Otrupcek R., 2001, *MNRAS*, **325**, 1213
- Woltjer L., 1972, *ARA&A*, **10**, 129
- Wu Z., et al., 2024, *arXiv e-prints*, p. arXiv:2406.12218
- Yao J., et al., 2021, *Nature Astronomy*, **5**, 788
- Zhu X.-J., Ashton G., 2020, *ApJ*, **902**, L12
- Özel F., Freire P., 2016, *Annual Review of Astronomy and Astrophysics*, **54**, 401–440

APPENDIX A: DISTANCE MEASUREMENTS TO PULSARS USING SCINTILLATION VELOCITIES

Here, we describe the information and methods required to determine an independent distance to a pulsar using scintillation. The modelling follows the Bayesian procedure outlined in Section 3.4. The required measurements include the scintillation bandwidth, $\Delta\nu_d$, timescale, $\Delta\tau_d$, phase gradient, ϕ , and an estimation of β from α' . These can be extracted from the dynamic spectra of pulsar observations.

Following Lambert & Rickett (1999), it is possible to calculate the uncertainty relation constant C_1 . This can be done by measuring the decorrelation bandwidth, $\Delta\nu_d$, and the scatter broadening timescale τ_s . One way to determine these properties is analytically by calculating the two-frequency plane-wave diffractive field coherence function, Γ_D , using, e.g., equation 59 in Lambert & Rickett (1999). This describes the scattering geometry and can be applied to spherical, plane waves, or those that propagate through an infinitely thin screen. This can be extended to account for anisotropy in a thin screen (Rickett et al. 2014, Equation A2). Within the SCINTOOLS package, we calculate the ACF of the electric field Γ_D using

$$\Gamma_D(\sigma, D_s; \nu, \Delta\nu) = \frac{\text{dsp}^2}{2\pi i \Delta\nu_n} \int_{-\infty}^{\infty} \int_{-\infty}^{\infty} \exp\left[-\frac{1}{2} D_\phi(\sigma'; \nu)\right] \times \exp\left[\frac{i}{2\Delta\nu_n} |\sigma - \sigma'|^2\right] d^2\sigma', \quad (\text{A1})$$

where dsp is a parameter that describes the resolution of the ACF and

$$\Delta\nu_n = \frac{2\pi\Delta\nu_d\nu^2 s_d^2}{D_s c} \quad (\text{A2})$$

defines the value of each frequency lag within our calculations (Reardon 2020).

This removes dependence on the distance, relative screen distance (D_s), scintillation bandwidth, and observing frequency. We compute the ACF of the scattered electric field by solving equation A1 at a grid of frequency and time lags. We calculate the ACF of the intensity by multiplying Γ_D by its complex conjugate. We then measure $\Delta\nu_d$ and τ_s as the frequency lag at which the correlation falls to one-half and the time lag at which it falls to $1/e$ of the peak value (Lambert & Rickett 1999). These are then used to determine C_1 using Equation 7. Code to calculate C_1 can be made available upon request.

Several parameters impact the form of Γ_D . These include the

spectral exponent, β , the axial ratio of anisotropy, A_R , the angle between the angle of anisotropy ζ and the direction of effective velocity $\mathbf{V}_{\text{eff}}(s)$, ψ , the normalised phase gradient, ϕ_n , and the angle between the phase gradient and the direction of $\mathbf{V}_{\text{eff}}(s)$, θ_ϕ . These parameters can be incorporated into codes that numerically integrate Equation A1 and model scintillation velocities.

For pulsars, particularly those in binary systems, it may not be appropriate to determine a single value of A_{ISS} . For example, Rickett et al. (2014) showed that the phase gradient of the IISM varied over the binary period of the double pulsar. It is often difficult to accurately measure ψ , ϕ_n , and θ_ϕ using scintillation measurements (Rickett et al. 2014; Reardon & Coles 2023), so their broad uncertainties need to be accounted for in the analysis.

It is therefore important to provide posterior distributions (or at least uncertainties) to constrain the parameters β , A_R , ζ , ψ , ϕ_n , and θ_ϕ when quantitatively assessing the geometric structure of scattering and the numerical value of C_1 and its uncertainty. A_{ISS} can be calculated from C_1 using Equation 6.

This value of A_{ISS} can then be inputted as a prior into the model for $\mathbf{V}_{\text{eff}}(s)$, which depends on D and s , among other parameters. Therefore, to determine D using scintillation the measurements, it is necessary to model $\mathbf{V}_{\text{eff}}(s)$. This model can be fitted to an effective velocity inferred from the dynamic spectrum, by sampling $\Delta\nu_d$ and $\Delta\tau_d$ across annual and orbital phases (if the pulsar is in a binary).

Alternatively, we can conduct this analysis by using the relationship between the spatial scale and scintillation bandwidth,

$$s_d = A_{\text{ISS}} \sqrt{D \Delta\nu_d} = \kappa \sqrt{\Delta\nu_d}, \quad (\text{A3})$$

where κ is the generalized constant of proportionality between s_d and $\Delta\nu_d$. Then we can solve for D using

$$D = \frac{\kappa^2}{A_{\text{ISS}}^2}. \quad (\text{A4})$$

We have measured the distance this way for the double pulsar when assuming $\alpha' = 4.4$ (Kolmogorov turbulence) as seen in Figure A1. This distance agrees with the VLBI distance from Kramer et al. (2021a). This demonstrates that scintillometry can provide comparable uncertainty to distance measurements from timing.

APPENDIX B: DATA QUALITY

To test how well our model describes our data, we assessed the Gaussianity of the residuals. The residuals are the difference between the data and model predictions, for scintillation time scales and velocities estimates. We did this using the cumulative distribution function shown in Figure B1. We expect the normalised residuals (the residuals divided by the uncertainties modified by noise parameters F and Q) to have a Gaussian distribution with zero mean and unit standard deviation. The expectation of such distribution is plotted in red, while the UHF, L-band and S-band measurements are plotted in orange, blue, and green, respectively. We undertook this test for both the $\Delta\tau_d^{-1}$ and V_{ISS} models. In the case of the V_{ISS} model, the UHF data were consistent with the Gaussian distribution, but the L-band and S-band data were not, which is why we only used the UHF data in subsequent analysis. In addition to this, we computed the Anderson Darling statistic (ADS; Anderson & Darling 1954), which can also be used to assess the Gaussianity of a data set. We measured a statistic of $\text{ADS} = 0.366$ for the $\Delta\tau_d^{-1}$ model. This was found to be smaller than the critical value for a normal distribution, suggesting

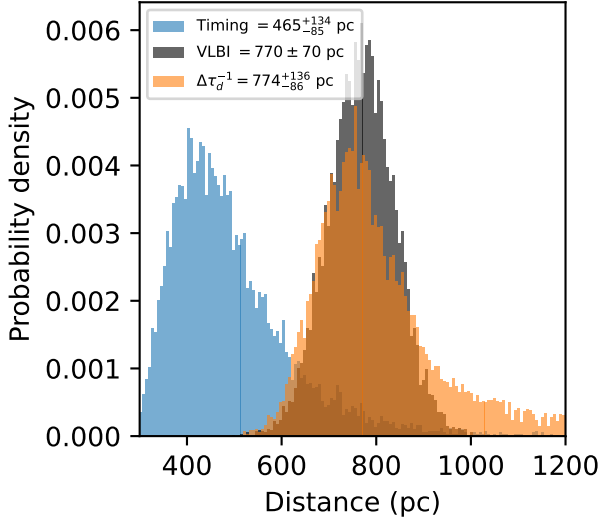


Figure A1. Distance measurements for the double pulsar system. The VLBI (black) and timing (blue) distributions were calculated from [Kramer et al. \(2021a\)](#). The scintillation distribution (orange) was calculated assuming Kolmogorov turbulence.

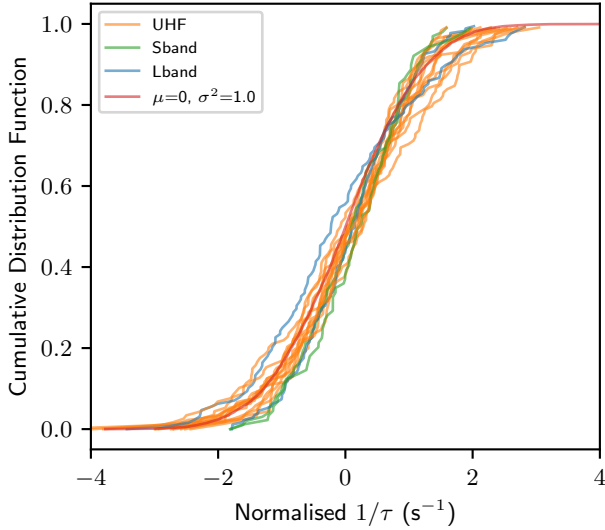


Figure B1. Cumulative distribution of inverse scintillation timescale measurements. We compare these to the normalised residuals from Figure 3. Each frequency band is shown using a different colour. They are all consistent with a normal distribution with a variance equal to unity.

that the distribution is consistent with a Gaussian distribution using this statistic as well.

This paper has been typeset from a \LaTeX file prepared by the author.